A 2D Pseudodynamic Rupture Model Generator for Earthquakes on Geometrically Complex Faults

by Daniel T. Trugman[*] and Eric M. Dunham

Abstract   Geologic observations indicate that faults are fractally rough surfaces, with deviations from planarity at all length scales. Fault roughness introduces complexity in the rupture process and resulting ground motion. We present a 2D kinematic rupture generator that emulates the strong dependence of earthquake source parameters on local fault geometry observed in dynamic models of ruptures on nonplanar faults. This pseudodynamic model is based on a statistical analysis of ensembles of 2D plane strain rupture simulations on fractally rough faults with rate-weakening friction and off-fault viscoplasticity. We observe strong anticorrelation of roughness-induced fluctuations in final slip, rupture velocity, and peak slip velocity with the local fault slope for right-lateral strike-slip ruptures. Spatial variability in these source parameters excites high-frequency seismic waves that are consistent with observed strong-motion records. Although accurate modeling of this high-frequency motion is critical to seismic-hazard analysis, dynamic rupture simulations are currently too computationally inefficient to be of practical use in such applications. We find that the seismic waves excited by the pseudodynamic model have similar intensity and spectral content to the corresponding dynamic model. Although the method has been developed in 2D, we envision that a similar approach could be taken for the 3D problem, provided that computational resources are available to generate an ensemble set of 3D dynamic rupture simulations. The resulting methodology is expected to find future application in efficient earthquake simulations that accurately quantify high-frequency ground motion.

Introduction

Simulations of strong ground motion form a crucial component of earthquake-hazard analysis. Earthquakes generate seismic waves over a wide range of frequencies, though much of the structural damage results from shaking close to the resonance frequency of the building in question. For most buildings (aside from tall high rises and long-span bridges), resonance frequencies fall in a range from ∼1 to 10 Hz, so the ability to accurately simulate ground motion within this frequency band is of great importance (O'Connell *et al.*, 2012). This high-frequency seismic radiation (> 1 Hz) is caused in large part by spatial and temporal variability in the earthquake rupture process (Haskell, 1966; Andrews, 1980; Mai and Beroza, 2002; Dunham *et al.*, 2011b). Earthquake simulations that can accurately generate realistic high-frequency motion would be particularly useful in supplementing empirical ground-motion estimates for near-field locations, where observational data are limited (Anderson and Brune, 1999; Abrahamson and Silva, 2008; Ripperger *et al.*, 2008).

Two distinct approaches to earthquake source modeling (kinematic and dynamic) are used to compute seismic ground motion. Kinematic models prescribe the time evolution of slip at each point along the fault interface (Aki and Richards, 2002; Boore, 2003; Hutchings, 1994, Madariaga, 2007). Typically, the earthquake source parameters that characterize kinematic models, such as the final slip and rupture velocity, are represented as spatial random fields (Herrero and Bernard, 1994; Mai and Beroza, 2002). These stochastic distributions introduce heterogeneity into the source model while maintaining spatial coherence of the source parameters. Combined with an assumed source–time function, which specifies the slip velocity as a function of time for a given point on the fault, these parameters completely define the kinematic earthquake source description.

Kinematic earthquake models are frequently applied in seismic-hazard analysis because they can be used to efficiently compute ground motion (Kostrov and Das, 1988; Aki and Richards, 2002). By leveraging reciprocity relationships, the prescribed kinematic slip boundary condition can be linearly convolved with the strain Green's tensor to rapidly generate synthetic seismograms at any location of interest (Zhao

---

*Now at Geophysics Group (EES-17), Los Alamos National Laboratory, P.O. Box 1663, Los Alamos, New Mexico 87545.

et al., 2006). Kinematic source models are a fundamental component of seismic-hazard assessments such as Cyber-Shake, which provides a probabilistic hazard assessment for the Los Angeles area of southern California (Graves, Jordan, *et al.*, 2011). CyberShake's kinematic source description is based on the *k*-square model (Herrero and Bernard, 1994), in which the slip spectrum follows a k^{-2} decay beyond a corner wavenumber k_c that is related to fault dimension. This source model is combined with community seismic velocity and fault models to efficiently compute ground motion in the Los Angeles region for a vast array of earthquake rupture scenarios. These ground-motion simulations, in turn, are aggregated to produce a hazard map, which quantifies the long-term probability of strong ground motion at different locations in the region.

One disadvantage of kinematic source modeling is that it requires an *a priori* assumption of the spatiotemporal slip distribution along the fault interface. For earthquake source models used to assess seismic hazard, it is crucial, therefore, that the earthquake source parameters used in a kinematic model both obey fundamental physical assumptions regarding fault friction and energetics, and realistically characterize the patterns of heterogeneity exhibited in real earthquakes (Schmedes *et al.*, 2012). However, geologic and seismic observations provide poor constraints on these source parameters, particularly the rupture velocity and the precise form of the source–time function (Song and Dalguer, 2013).

Earthquake rupture simulations using dynamic source models can provide insight into the development of realistic source parameters. Rather than assuming a particular slip distribution and source–time function, as in kinematic models, dynamic models explicitly simulate the earthquake rupture process, thus obtaining the time evolution of fault slip directly (Freund, 1990; Aki and Richards, 2002; Wang, 2008). Dynamic models specify a particular frictional failure law, such as a slip-weakening model in which the frictional stress of the fault drops from its static to dynamic value as the fault slips. The rupture can be simulated by numerically solving the elastodynamic equations with the assumed friction law and stress boundary conditions along the fault interface (Andrews, 1976; Das and Aki, 1977; Day, 1982).

Because dynamic models are physically self consistent, they can provide important constraints on earthquake source parameters. However, the explicit modeling of the rupture process is an inherently nonlinear computational problem, preventing the use of elastic reciprocity relations to increase efficiency. Dynamic simulations are therefore much more computationally intensive than simulations using reciprocity-based kinematic models, which require only the linear operation of convolution with the strain Green's tensor to compute ground motion (Kostrov and Das, 1988; Zhao *et al.*, 2006). Because of this, dynamic models are currently of limited utility in probabilistic seismic-hazard assessments. They are too inefficient to generate the large array of simulations required to quantify probability distributions for strong ground motion in scenario earthquakes. For example, CyberShake uses, on average, 415,000 different rupture variations for each of over 200 site locations in the Los Angeles region to construct its hazard maps (Graves, Jordan, *et al.*, 2011). This is a formidable computation task, even using highly optimized and efficient kinematic source models.

Most dynamic earthquake simulations to date use an idealized, planar fault geometry while imposing stochastic heterogeneity to the stress boundary conditions or frictional parameters (e.g., Oglesby and Day, 2002; Guatteri *et al.*, 2003; Ripperger *et al.*, 2007). However, much of the heterogeneity in earthquake source parameters can be attributed to the geometric complexity of the fault surface (Andrews, 1980). Measurements of natural faults indicate that fault surfaces are self-similar fractals that exhibit roughness at all length scales (Brown and Scholz, 1985; Lee and Bruhn, 1996; Sagy and Brodsky, 2009; Candela *et al.*, 2012).

Dunham *et al.* (2011b) studied the effect of fractally rough fault geometry in dynamic rupture simulations. Their 2D plane strain model assumes a uniform initial stress field in the medium and a strongly rate-weakening friction law. Off-fault viscoplasticity is applied to limit unreasonably large stress concentrations near bends in the fault and to eliminate fault opening. Rupture propagation under these assumptions gives rise to self-healing slip pulses for near-critical levels of background shear stress (Zheng and Rice, 1998).

In their simulations, Dunham *et al.* (2011b) found that roughness-induced stress perturbations give rise to heterogeneity in final slip and rupture velocity. Fluctuations in these source parameters exhibit strong dependence on the local fault geometry. In the case of right-lateral strike-slip rupture and orientations of principal stresses consistent with strike-slip faulting, the authors observed strong anticorrelation of both final slip and rupture velocity with fault slope. As the fault bends into a compressional quadrant (as defined by the far-field *P*-wave first motions), the rupture decelerates and slip is suppressed (Fig. 1). Conversely, as the fault bends into an extensional quadrant, the rupture accelerates and slip is enhanced. In this way, the nonplanar fault geometry introduces correlations between earthquake source parameters.

Furthermore, Dunham *et al.* (2011b) found that these dynamic source models excite seismic waves with spectral properties that are consistent with ground-motion records. More recent 3D rough-fault simulations by Shi and Day (2013) are even more convincing, generating acceleration response spectra that are comparable to empirical estimates over a wide range of frequencies. Observations of far-field ground motion show that the shear-wave acceleration power spectral density is independent of frequency over a band of frequencies ranging from a lower limit at the corner frequency f_0, to an upper limit $f_{\max}$, the maximum frequency that is insensitive to attenuation along the source-to-site ray path (Hanks and McGuire, 1981). Although observations of near-field (i.e., the region within about one source dimension of the fault) ground motion are limited, Andrews (1981) demonstrated that near-field ground motion should exhibit a similar flat power spectrum at high frequency.
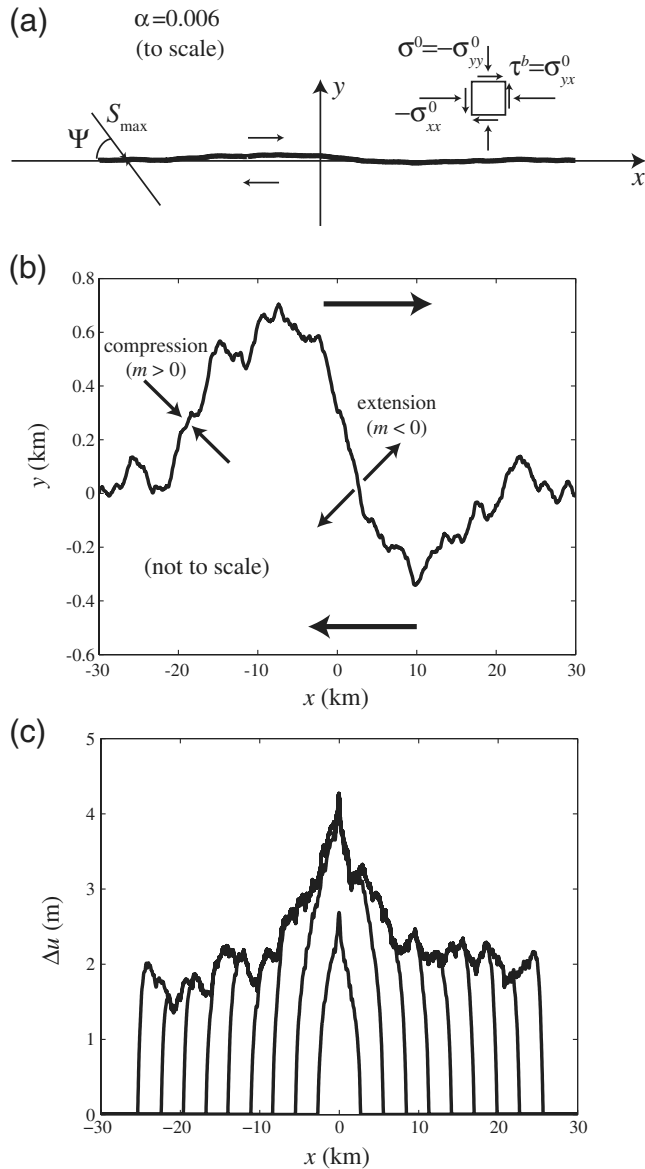
Figure 1. (a) Plane strain model for dynamic rupture simulations, with right-lateral slip on a bandlimited self-similar fault ($\alpha = 0.006$). The stress state is spatially uniform, with the maximum compressive principal stress inclined at an angle of $\Psi = 50°$ to the fault. Fault profile plotted to scale. (b) Fault profile exaggerated in the y direction to show fluctuations. Examples of compressional and extensional bends in the fault profile are also labeled. (c) Evolution of slip $\Delta u(x)$ along the same fault profile for a typical dynamic rupture simulation (background shear stress $\tau_b = 38.5$ MPa, $\tau_b/\sigma_0 = 0.3056$). The time interval between adjacent contours is 1 s.

Because accurate constraints on high-frequency ground motion are one of the most important aims of probabilistic seismic-hazard analysis (PSHA), it would be desirable to utilize physically consistent dynamic rupture simulations like those studied by Dunham *et al.* (2011b) in the quantification of seismic hazard. Unfortunately the computational cost of such dynamic simulations precludes their direct application to PSHA at the present time. However, a hybrid kinematic–

dynamic, or pseudodynamic, model that maps the key physical properties of rupture simulations on nonplanar faults to a computationally efficient kinematic model could provide substantial improvement to the current suite of ground-motion prediction techniques.

In this study, we develop such a pseudodynamic earthquake source model in 2D. We begin with a statistical analysis of the earthquake source parameters for an ensemble of 2D dynamic rupture simulations on fractally rough faults. Analogous pseudodynamic models have been developed through study of stochastic dynamic rupture simulations on planar faults (e.g., Guatteri *et al.*, 2004; Schmedes *et al.*, 2012). These models are based on the observations of dynamic models that represent stress heterogeneities as spatial random fields with a power law spectral decay, as proposed by Andrews (1980). Other similar models have been developed that assume spatial correlations between the kinematic source parameters (e.g., Liu *et al.*, 2006; Song *et al.*, 2009; Song and Somerville, 2010). For example, Liu *et al.* (2006) developed an earthquake source model that features a positive correlation between the final slip and the rupture velocity at a given point on the fault. Mena *et al.* (2012) found that the presence of asperities (regions of high-stress drop) provides a strong control on both the slip distribution and local rupture velocity, and their pseudodynamic model accounts for possibility of rupture velocities exceeding the local shear-wave speed.

Though dynamic simulations are useful in the process of developing physically consistent earthquake source parameters, it must be emphasized that the dynamic models themselves cannot perfectly represent the intricate physics of earthquake rupture. Stochastic dynamic models are subject to epistemic uncertainty because field observations of earthquakes do not provide strong constraints on the spatial heterogeneity of the background stress field (Schmedes *et al.*, 2010; Song and Dalguer, 2013). It is entirely possible, therefore, to develop a pseudodynamic model that emulates the basic properties of an ensemble of dynamic earthquake simulations, but not those of natural earthquakes.

In contrast to the pseudodynamic models developed from traditional stochastic dynamic simulations, the basis of the spatial patterns in source parameters in our pseudodynamic source model is a direct observable—fault roughness. This mitigates one important source of epistemic uncertainty present in previous pseudodynamic models (though uncertainties in other parameters, such as those related to the assumed friction law, remain). In our pseudodynamic rupture model, we first generate a random, fractally rough fault profile with root mean square (rms) deviations from planarity that are proportional to the profile length. Roughness is only included at wavelengths much larger than the scale of slip. Based on the analysis of the earthquake source parameters observed in dynamic rupture simulations on such fault profiles, our pseudodynamic rupture generator models the distributions of final slip, rupture velocity, and peak slip velocity as spatial random fields, which are anticorrelated with the

local fault slope. These parameters are then used to establish a source–time function for each point along the 2D fault interface. With this pseudodynamic source model, we compute synthetic seismograms by simply resolving this source–time function along the nonplanar fault and applying the representation theorem. We then compare the results of this model both with a dynamic rupture nucleated on the same profile, as well as with an identical version of the pseudodynamic model resolved along a planar fault. Doing so allows us to isolate the effect of fault orientation on the seismic wavefield, with the earthquake source parameters held fixed. Finally, we compare ensembles of dynamic and pseudodynamic models to confirm that the observed similarity in ground motion is independent of the specific random realization of the fault profile.

Model Description

Dynamic rupture simulations provide the necessary constraints for the statistical properties of our pseudodynamic earthquake source model. In this section, we begin by summarizing the relevant characteristics of the 2D plane strain model and fractally rough fault geometry used in these dynamic simulations. We next compute ensemble averages for the correlation coefficients between the local fault slope and three earthquake source parameters: final slip, rupture velocity, and peak slip velocity. The correlations of these three earthquake source parameters, along with ensemble averages of their respective autocorrelation functions, form the basis for the pseudodynamic model.

Dynamic Rupture Simulations on Rough Faults

Consider a 1D fault profile:

$$y = h(x), \qquad (1)$$

with zero mean and local fault slope:

$$m(x) = \frac{dh}{dx}. \qquad (2)$$

The rms roughness of a fault band limited between wavenumbers of $k_{\min}$ and $k_{\max}$ is

$$h_{\mathrm{rms}}(k_{\min}, k_{\max}) = \sqrt{\frac{1}{\pi} \int_{k_{\min}}^{k_{\max}} P_h(k)\,dk}, \qquad (3)$$

in which $P_h(k)$ is the power spectral density of the fault profile $h(x)$. For a fault that is self-similar, $P_h(k)$ can be written in the form

$$P_h(k) = (2\pi)^3 \alpha^2 |k|^{-3}, \qquad (4)$$

in which the parameter α is the amplitude-to-wavelength ratio of the fault profile. For a fault of length L, in the limit $k_{\min} \to 2\pi/L$ and $k_{\max} \to \infty$, $h_{\mathrm{rms}} = \alpha L$. The rms rough-

ness is therefore proportional to the profile length. For natural faults, α is of order 10^{-3} to 10^{-2} for roughness in the slip-parallel direction (Power and Tullis, 1991), the relevant case in our 2D strike-slip models. Further details of the mathematical properties of such self-affine fault profiles are given in Dunham et al. (2011b) and Candela et al. (2012).

Some studies indicate that natural faults become progressively less rough as slip accumulates (Sagy and Brodsky, 2009). However, Candela et al. (2012) argue that eventually, a dynamic equilibrium is achieved in which the processes that increase fault roughness (e.g., dynamic branching of ruptures onto secondary faults) are balanced by those that reduce fault roughness (e.g., wear due to slip). Self-similar fault profiles like the ones implemented in our simulations are representative of a single fault segment. We neglect the possibility of ruptures branching onto secondary fault surfaces, or arresting at junctures between adjacent fault segments. One can envision extending both the dynamic and pseudodynamic models to account for branches and stepovers, with appropriate quantification of the likelihood of multisegment ruptures. However, that task is beyond the scope of this initial study.

Figure 1 outlines the initial configuration of a typical dynamic model. We first generate a fault profile by filtering a Gaussian-distributed random vector in the frequency domain to attain a profile with the spectral properties of equation (4). To ensure numerical accuracy, roughness is restricted to wavelengths between $\lambda_{\min} = 30\Delta x$ and the profile length L. We use grid spacing $\Delta x = 10$ m and $L = 60$ km, hence $\lambda_{\min} = 300$ m for our simulations, which suffices to excite high-frequency waves up to about 10 Hz. The initial stress field, σ_{ij}^0, is spatially uniform, and can be completely defined relative to the plane $y = 0$ by the initial background shear stress, $\tau^b = \sigma_{yx}^0$, the effective normal stress, $\sigma^0 = -\sigma_{yy}^0$, and the angle Ψ between the maximum compressive principal stress and $y = 0$. Although the stress field is spatially uniform, the nonplanarity of the fault creates heterogeneity in the local stress tractions resolved along the fault profile. Slip on the nonplanar fault introduces further stress heterogeneity during the rupture process.

Our dynamic rupture simulations employ a rate-and-state friction law, for which the coefficient of friction evolves over a characteristic slip distance to a rate-weakening steady state. Rate-weakening friction is ubiquitous in laboratory studies (e.g., Tsutsumi and Shimamoto, 1997; Di Toro et al., 2004; Beeler et al., 2008), and for sufficiently low-background shear stress τ^b (specifically, $\tau^b \sim \tau^{\mathrm{pulse}}$ for ruptures on a planar fault in a purely elastic medium), allows for the self-healing slip pulses desired in earthquake simulations (Zheng and Rice, 1998; Fang and Dunham, 2013). The off-fault medium obeys noncohesive elastic–viscoplastic Drucker–Prager rheology, which mitigates fault opening and prevents unreasonably large stress concentrations at geometric bends in the fault profile (Dunham et al., 2011b).

Ruptures are nucleated by applying an abrupt stress perturbation over an $\sim$300 m region surrounding the desired

hypocenter. This hypocentral location could, in principle, be chosen at random. However, we expect that real earthquakes nucleate in locations where the resolved shear-to-normal stress ratio, τ/σ is high. Because earthquake nucleation requires that rupture energetics are favorable over a finite source region (Dieterich, 1992), we choose our hypocenter to be the location of maximal smoothed τ/σ, as described in Fang and Dunham (2013). Thus, the hypocenter is positioned within a long-wavelength extensional zone along the profile, in which the local fault geometry favors spontaneous rupture. For computational purposes, we then shift the profile and redefine our coordinate system so the nucleation zone is centered about $x = 0$.

Earthquake Source Parameters in Dynamic Simulations

Kinematic models require the specification of a source–time function at each point along the fault interface. With this in mind, we focus our statistical analysis of dynamic ruptures on the spatiotemporal properties of fault slip. Specifically, we consider three scalar source parameters—final slip Δu, local rupture velocity v_{rup}, and peak slip velocity V_{peak}—and study how these parameters depend on local fault slope, $m(x)$. Note that many kinematic earthquake models specify the rise time (the duration of slip) rather than V_{peak} as we do (e.g., Schmedes *et al.*, 2012). Either is sufficient for our purposes, and as shown below, V_{peak} turns out to be more convenient to work with in this context.

We fix the roughness parameter α to an intermediate value of 0.006 and principal stress angle Ψ to 50°. As observed by Dunham *et al.* (2011b), the correlation of the source parameters with local fault slope depends on Ψ, which must be sufficiently large such that yielding occurs only on one side of the fault profile. The following analysis is based on an ensemble of 329 dynamic simulations (Fang and Dunham, 2013) with background shear stress level τ^b ranging from 35.3 to 42.5 MPa, with σ^0 held fixed at 126 MPa. For low τ^b/σ^0, ruptures are barely sustainable and most fail to grow to a significant length (Zheng and Rice, 1998; Dunham *et al.*, 2011b), whereas large τ^b/σ^0 commonly induces ruptures with supershear propagation speeds, at which the local rupture velocity exceeds the shear wavespeed.

As explained by Dunham (2007) and Liu and Lapusta (2008), a supershear transition can occur as the rupture front moves from a region of high strength to a region of low strength. In this situation, the shear stress peak leading the rupture from the seismic radiation can exceed the local peak strength of the fault, forming a daughter crack, or simply accelerating the main rupture front in a continuous manner to a supershear speed. In the context of our 2D rupture simulations, supershear transitions can therefore occur as the rupture front moves from a compressional (high strength) to an extensional (low strength) region, due to changes in fault geometry. The likelihood of supershear transition increases with τ^b/σ^0, in general agreement with the observation of

Mena *et al.* (2012) that the supershear rupture velocities are more pervasive in dynamic simulations with longer rupture length (which tend to occur, in our simulations, at higher-background stress levels). Although the supershear transition is an interesting problem in its own right, it vastly complicates the distributions of our earthquake source parameters, and will be neglected in the proceeding analysis. We limit our focus to the intermediate values of τ^b/σ^0 that result in self-sustaining, subshear self-healing slip pulses.

Kinematic rupture generators typically model earthquake source parameters as spatial random fields (e.g., Mai and Beroza, 2002). Each spatial random field can be defined by a marginal distribution and an autocorrelation function, which characterize the random field's one-point and two-point statistics, respectively (Christakos, 1992; Song and Somerville, 2010; Song and Dalguer, 2013). The marginal distribution for a parameter is the probability density function for that parameter at a single point along the fault, whereas the autocorrelation function captures the spatial coherence of the random field. More formally, for a stationary, 1D function of a random variable, $f(x)$, the normalized autocorrelation function, $R_f(x)$, is defined as

$$R_f(x) = \frac{E\{[f(\xi) - \mu_f][f(\xi + x) - \mu_f]\}}{\sigma_f^2}, \qquad (5)$$

in which μ_f and σ_f are the mean and standard deviation of f, and the operation $E\{\bullet\}$ denotes the expectation value. It is convenient to use normalized autocorrelation functions in this context, as it allows the marginal distribution to completely define the one-point statistics (e.g., μ_f and σ_f) for the spatial random field. The normalized power spectral density is the frequency domain analog to the autocorrelation function:

$$P_f(k) = \int_{-\infty}^{\infty} R_f(x) \exp(-ikx)dx. \qquad (6)$$

In forming our pseudodynamic rupture model, we seek to approximate the dynamic model source parameters as spatial random fields. This requires a choice of both a marginal distribution and an autocorrelation function to fit to the data from the ensemble of dynamic simulations. For this preliminary study, we choose a simple Gaussian marginal distribution:

$$f(x) = \frac{1}{\sigma\sqrt{2\pi}} \exp\left[\frac{-(x - \mu)^2}{2\sigma^2}\right], \qquad (7)$$

with mean μ and standard deviation σ, and exponential autocorrelation function,

$$R_f(x) = \exp(-|x|/a_c), \qquad (8)$$

with correlation length a_c. Although Gaussian marginal distributions and exponential autocorrelation functions are commonly used to define spatial random fields, they are by no

Table 1

Dynamic Simulation Statistics for Final Slip, Δu

$\tau_b{}^*$ (MPa)	Δu (mean) (m)	Δu (S.D.[†]) (m)	$r_{m,u}{}^{‡}$	$a_{c,u}{}^{§}$ (km)	$\xi_u{}^{\parallel}$ (km)
35.3	1.24	0.19	−0.76	0.69	0.03
36.5	1.55	0.29	−0.73	0.90	0.03
37.5	1.72	0.38	−0.69	1.17	0.03
38.5	1.98	0.39	−0.69	1.18	0.02
41.5	2.86	0.63	−0.65	1.57	0.02
42.5	3.24	0.78	−0.63	1.72	0.02

*Background shear stress.

[†]Final slip standard deviation (S.D.)

[‡]Zero-offset cross-correlation coefficient between fault slope m and final slip Δu.

[§]Correlation length for final slip Δu.

[∥]Offset distance for maximal cross correlation between fault slope m and final slip Δu.

Table 2

Dynamic Simulation Statistics for Rupture Velocity, v_{rup}

$\tau_b{}^*$ (MPa)	v_{rup}/c_s (mean)[†]	v_{rup}/c_s (S.D.)[‡]	$r_{m,vr}{}^{§}$	$a_{c,vr}{}^{\parallel}$ (km)	$\xi_{vr}{}^{\#}$ (km)
35.3	0.81	0.05	−0.67	0.04	−0.06
36.5	0.83	0.11	−0.65	0.06	−0.05
37.5	0.83	0.10	−0.67	0.14	−0.05
38.5	0.83	0.07	−0.68	0.16	−0.05
41.5	0.84	0.09	−0.67	0.40	−0.03
42.5	0.85	0.16	−0.67	0.42	−0.03

*Background shear stress.

[†]Rupture velocity v_{rup} normalized by shear wavespeed c_s.

[‡]Rupture velocity v_{rup} standard deviation (S.D.)

[§]Zero-offset cross-correlation coefficient between fault slope m and rupture velocity v_{rup}.

[∥]Correlation length for rupture velocity v_{rup}.

[#]Offset distance for maximal cross correlation between fault slope m and rupture velocity v_{rup}.

Table 3

Dynamic Simulation Statistics for Peak Slip Velocity, V_{peak}

$\tau_b{}^*$ (MPa)	V_{peak} (mean) (m/s)	V_{peak} (S.D.)[†] (m/s)	$r_{m,V_p}{}^{‡}$	$a_{c,V_p}{}^{§}$ (km)	$\xi_{V_p}{}^{\parallel}$ (km)
35.3	12.82	1.13	−0.90	0.37	0.00
36.5	13.17	1.25	−0.83	0.38	0.00
37.5	13.36	1.27	−0.82	0.54	0.00
38.5	13.73	1.11	−0.82	0.61	0.00
41.5	14.44	1.18	−0.78	1.07	0.00
42.5	14.65	1.24	−0.76	1.24	0.00

*Background shear stress.

[†]Velocity standard deviation (S.D.)

[‡]Zero-offset cross-correlation coefficient between fault slope m and peak slip velocity V_{peak}.

[§]Correlation length for peak slip velocity V_{peak}.

[∥]Offset distance for maximal cross correlation between fault slope m and peak slip velocity V_{peak}.

means the unique choice. Mai and Beroza (2002), for example, concluded that a von Karman autocorrelation function provided a good fit for empirical slip data, whereas Lavallée et al. (2006) found that the generalized Lévy distribution (which has an additional free parameter compared with a von Karman distribution) better characterized the statistical properties of final slip. Future work could generalize our pseudodynamic model to incorporate other marginal distributions (using a simple normal score transform, as outlined by Liu et al., 2006), as well as alternative autocorrelation functions.

For the purposes of this pseudodynamic model, however, we assume that the three source parameters can be approximated as spatial random fields with Gaussian marginal distributions and exponential autocorrelation functions. Though the exponential autocorrelation function provides a good fit to the data from our dynamic ensemble, the assumption of Gaussian marginal distributions has important ramifications on the seismic wavefield, as will be discussed further in the Results section.

We further assume that the marginal distributions are stationary, that is, independent of the position along the profile. To assess the limits of this assumption, Figure 1c plots final slip Δu, along a fault profile for a typical rupture with $\tau^b = 38.5$ MPa ($\tau^b/\sigma^0 = 0.3056$). While short-wavelength variations in slip are visibly present, the artificial nucleation procedure causes a noticeable peak in the magnitude of Δu near the hypocenter. Because the nucleation effects tend to dominate the effects of fault geometry in this region, we conservatively restrict our analysis to distances of $|x| > 10$ km, well away from the hypocenter. In these sectors, the marginal distributions for the three source parameters are approximately stationary. Further work could be done to incorporate nonstationary marginals into future pseudodynamic rupture models by applying, for example, a distance binning process as described by Schmedes et al. (2012).

Tables 1, 2, and 3 outline the results of fitting these distributions to our ensemble of dynamic rupture simulations.

Mean values of final slip Δu (Table 1) and peak slip velocity V_{peak} (Table 3) tend to increase with increasing background shear stress, τ^b, as anticipated. Rupture velocity v_{rup} (Table 2), is roughly independent of stress level, with mean value of 0.83 times c_s, the shear wavespeed. This result is consistent with both field data and previous analysis of dynamic rupture simulations (Somerville, 1999; Schmedes et al., 2010). Recall that we exclude any ruptures, which exhibit a supershear transition from this analysis. Had we not done so, the mean and standard deviation values for v_{rup} would be considerably higher, and the marginal distribution would be bimodal rather than unimodal, with peaks at both subshear and supershear rupture velocities.

Also of interest are the relative magnitudes of the correlation length a_c for the different source parameters. Final slip Δu is the most spatially coherent, with the autocorrelation exponentially decaying over a distance on the order of 1.2 km. In contrast, V_{peak} decays over a distance on the order of 0.7 km, whereas v_{rup} is the least spatially coherent, with

the autocorrelation falling off over about 0.2 km. The state evolution region of the rupture front, over which the strength drop occurs (Dunham *et al.*, 2011b), is characterized by a length scale $R_0 = 0.3$ km. This is comparable in magnitude to the correlation length for rupture velocity, but smaller than the correlation lengths of peak slip velocity and final slip. Thus, spatial correlations in rupture velocity do not extend beyond the finite size of the rupture front.

This local control of rupture velocity is a pervasive feature of dynamic simulations that manifest in the self-healing slip pulse rupture mode. Crack-like rupture simulations employing a slip-weakening friction law show more dependence on the history of stress drop along the fault (Fukuyama and Madariaga, 1998; Guatteri *et al.*, 2003), as compared to pulse-like ruptures with strongly rate-weakening friction (Zheng and Rice, 1998). A recent study by Gabriel *et al.* (2012) thoroughly explores the parameter space of initial stresses and frictional conditions that lead to crack-like and pulse-like ruptures. In the context of our ensemble of dynamic rupture simulations, stress perturbations are controlled entirely by fault roughness, which has a minimum wavelength $\lambda_{\min} = 0.3$ km that is comparable to the correlation length of 0.2 km for $v_{\rm rup}$. Rupture velocity therefore appears to respond to the short-wavelength perturbations in fault roughness, whereas peak slip velocity and final slip respond over longer length scales.

Furthermore, the correlations length a_c tends to increase with τ^b for all three source parameters. Simulations with τ^b/σ^0 just above the critical threshold for self-sustaining slip pulses tend to have low values of a_c, implying less spatial coherence and a more localized control of rupture growth by fault geometry. Conversely, ruptures with elevated τ^b/σ^0 are more spatially coherent, with large values of a_c. This is consistent with the conclusions of Zheng and Rice (1998) that ruptures with low-background shear stress are self-healing slip pulses (assuming rate-weakening friction), whereas those under high stress are crack-like, and hence have source parameters with longer correlation lengths.

In the analysis thus far, we have not considered the spatial interdependence of the source parameters. However, the crucial feature of our pseudodynamic model is that the source parameters are strongly correlated with the local fault geometry. To capture this behavior, we first need to define the zero offset, normalized correlation coefficient of two functions $f(x)$ and $g(x)$:

$$r_{f,g} = E\{[f(x) - \mu_f][g(x) - \mu_g]\}/(\sigma_f \sigma_g). \quad (9)$$

The correlation coefficient can take on any value on the closed interval $[-1, 1]$, and is a measure of the strength of the linear relation between the two functions. Conceptually, positive r implies that the local maxima and minima of the two functions tend to be aligned as a function of x, whereas negative r implies that these extrema are antialigned. Equation (9) generalizes to the case of nonzero offset:

$$r_{f,g}(\xi) = E\{[f(x) - \mu_f][g(x + \xi) - \mu_g]\}/(\sigma_f \sigma_g), \quad (10)$$

with the $r(\xi)$ denoting the correlation at spatial offset ξ.

Tables 1–3 list values of r_m, the zero-offset correlation with fault slope $m(x)$, for the three source parameters in our dynamic ensemble. Final slip Δu, rupture velocity $v_{\rm rup}$, and peak slip velocity $V_{\rm peak}$ all exhibit pronounced anticorrelation with fault slope $m(x)$. Correlation coefficients, averaged across all τ^b considered, are ~ -0.7 for Δu and $v_{\rm rup}$, and ~ -0.8 for $V_{\rm peak}$. Positive $m(x)$ causes the rupture to move into an increasingly compressional environment, causing the rupture to slow down (Fig. 1b). Figure 2 provides visual evidence of the strong anticorrelation of slope with the three source parameters. Local maxima in fault slope match up with minima in the source parameter magnitude, and vice versa. Similar connections between source parameters and fault geometry have been made in field observations of earthquakes (Oglesby *et al.*, 2008; Wesnousky, 2008), though at much longer length scales than those resolved by our dynamic rupture simulations. We find that rise time (defined as the time from 5% to 95% total slip) is not strongly correlated with fault slope ($r_m \sim -0.3$). Because of this, rise time is not explicitly used as a source parameter in our pseudodynamic rupture model. For completeness, we include in Table 4 ensemble averages for the zero-offset cross-correlation coefficients between the three source parameters. Like rise time, these correlations are not explicitly considered in our rupture generator.

Additionally, Tables 1–3 list the values for $\xi_{\max}$, the offset ξ that maximizes the correlation between $m(x)$ and the three source parameters:

$$\xi_{\max} = \arg \max_{\xi} |r_m(\xi)|. \quad (11)$$

Positive values of $\xi_{\max}$ indicate that shifting the source parameter toward the hypocenter, relative to $m(x)$, maximizes $|r_m(\xi)|$, whereas negative values of $\xi_{\max}$ indicate that shifting the source parameter away from the hypocenter maximizes $|r_m(\xi)|$. We find that $\xi_{\max}$ is relatively small in value for all three source parameters. $v_{\rm rup}$ has the most pronounced difference in cross correlation, with a forward shift of $\sim$50 m resulting in a substantial increase in correlation. Although final slip Δu has the maximum cross correlation with a backward shift of $\sim$20 m, the correlation is only very slightly increased with this offset. $V_{\rm peak}$ has the maximum correlation at zero offset. These results can be explained in terms of the relative spatial coherence of the different source parameters. In particular, rupture velocity is sensitive to short-wavelength fluctuations in fault slope. Although perturbations in fault slope create instantaneous perturbations in the traction along the fault profile, the rupture cannot slow down instantaneously, causing $v_{\rm rup}(x)$ to lag $m(x)$. $V_{\rm peak}$ and Δu are more spatially coherent than $v_{\rm rup}$ and thus do not demonstrate similar lag effects.
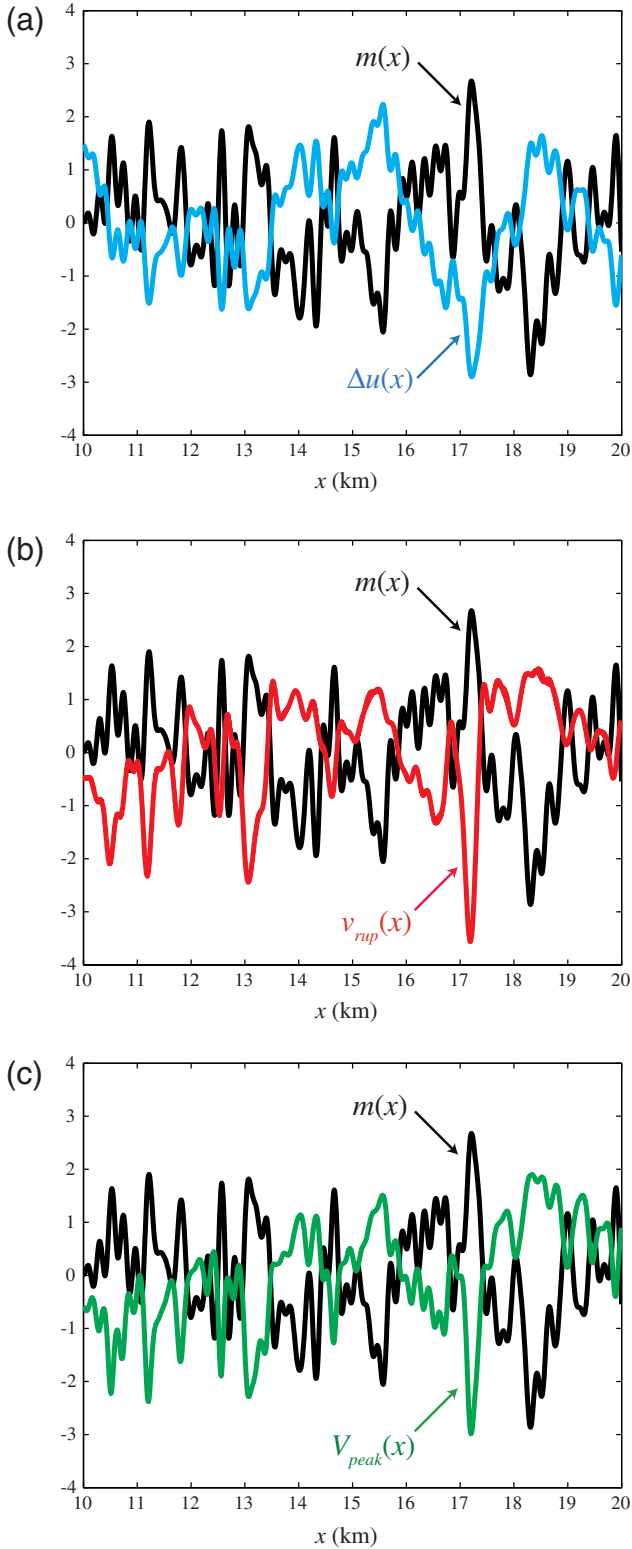
(a)

(b)

(c)

Figure 2. Relationship between source parameters and fault slope $m(x)$ for the same dynamic rupture simulation as in Figure 1. The slope and source parameters have been normalized and are plotted in units of standard deviations from their respective mean values. (a) Normalized $m(x)$ versus normalized $\Delta u(x)$. (b) Normalized $m(x)$ versus normalized $v_{\mathrm{rup}}(x)$. (c) Normalized $m(x)$ versus normalized $V_{\mathrm{peak}}(x)$. The color version of this figure is available only in the electronic edition.

Table 4
Correlations between Dynamic Simulation Source Parameters

τ_b* (MPa)	$r_{u,vr}$[†]	r_{u,V_p}[‡]	r_{vr,V_p}[§]
35.3	0.53	0.86	0.78
36.5	0.46	0.74	0.69
37.5	0.49	0.73	0.75
38.5	0.50	0.72	0.76
41.5	0.55	0.75	0.75
42.5	0.53	0.73	0.73

*Background shear stress.
[†]Zero-offset cross-correlation coefficient between final slip Δu and rupture velocity v_{rup}.
[‡]Zero-offset cross-correlation coefficient between final slip Δu and peak slip velocity V_{peak}.
[§]Zero-offset cross-correlation coefficient between rupture velocity v_{rup} and peak slip velocity V_{peak}.

Development of a Pseudodynamic Rupture Generator

Our pseudodynamic model represents the three source parameters—final slip Δu, local rupture velocity v_{rup}, and peak slip velocity V_{peak}—as spatial random fields that are consistent with the observed statistics of the dynamic simulations. Because we are interested in directly comparing the excited ground motion of dynamic and pseudodynamic models, we fix the background stress at an intermediate level of 38.5 MPa, and use the dynamic ensemble statistics for that stress level as the basis of the pseudodynamic model.

The first step in building this pseudodynamic model is to generate the bandlimited, fractally rough, fault profile. As described in the dynamic model description, this involves filtering a vector of Gaussian-distributed random numbers in the frequency domain to achieve the desired power spectral density given by equation (4). The output of this process is simply the fault profile, $y = h(x)$.

For the pseudodynamic model, we also need the earthquake source parameters along the profile, as a function of x: $\Delta u(x)$, $v_{\mathrm{rup}}(x)$, and $V_{\mathrm{peak}}(x)$. To obtain these functions (which are mapped to vectors on our finite numerical grid), we generate three additional vectors of Gaussian random numbers. These random vectors are not, however, independent—they are correlated with the fault profile vector. To achieve these correlations, we proceed as described by Liu *et al.* (2006).

Let $\mathbf{N}_h$, $\mathbf{N}_u$, $\mathbf{N}_{vr}$, $\mathbf{N}_{V_p}$ denote the initial Gaussian random vectors for the profile and the three source parameters, respectively, and let r_u, r_{vr}, and r_{V_p} denote the desired correlations of the parameters with the fault slope. The initial random vectors for the source parameters can then be correlated with the fault profile as follows:

$$\mathbf{N}'_u = r_u \mathbf{N}_h + \sqrt{1 - r_u^2}\,\mathbf{N}_u$$

$$\mathbf{N}'_{vr} = r_{vr} \mathbf{N}_h + \sqrt{1 - r_{vr}^2}\,\mathbf{N}_{vr}$$

$$\mathbf{N}'_{V_p} = r_{V_p} \mathbf{N}_h + \sqrt{1 - r_{V_p}^2}\,\mathbf{N}_{V_p}, \tag{12}$$

in which $\mathbf{N}'_u$, $\mathbf{N}'_{vr}$, and $\mathbf{N}'_{V_p}$ denote the correlated vectors of the three source parameters. Formally, these earthquake source parameters should be correlated with the vector corresponding to the spatial random field $m(x)$, the fault slope, rather than $h(x)$, the fault profile. However, because $m(x) = dh/dx$, it can be shown that $P_m(k) = k^2 P_h(k)$. Thus, we can generate consistent $h(x)$ and $m(x)$ from the same input random vector.

Once $\mathbf{N}'_u$, $\mathbf{N}'_{vr}$, and $\mathbf{N}'_{V_p}$ are computed, these correlated vectors can then be transformed into spatial random fields in a process analogous to that used to generate the profile itself, except with the power spectral density given by taking the Fourier transform of equation (8):

$$P(k) = \int_{-\infty}^{\infty} R(x) \exp(-ikx) dx$$
$$= \int_{-\infty}^{\infty} \exp(-|x|/a_c) \exp(-ikx) dx$$
$$= \frac{2/a_c}{k^2 + a_c^{-2}}. \qquad (13)$$

Our pseudodynamic model uses the values appropriate for $\tau^b = 38.5$ MPa listed in Tables 1–3 for the correlation coefficients r_m and correlation lengths a_c of each source parameter. These spatial random fields, which have zero mean and unit variance, are then scaled so that they have mean values and standard deviations consistent with those listed in Tables 1–3. Finally, $v_{\text{rup}}(x)$ is shifted by 0.05 km away from the hypocenter, as is observed in our dynamic ensembles.

To complete the pseudodynamic model, we must convert the three source parameters into a source–time function for each point along the fault profile. The rupture time $t_{\text{rup}}(x)$ can be computed by integrating the reciprocal of $v_{\text{rup}}(x)$:

$$t_{\text{rup}}(x) = \int_0^x v_{\text{rup}}^{-1}(x') dx'. \qquad (14)$$

Thus, $t_{\text{rup}}(x)$ is the time at which fault slip commences along the profile, as a function of x. We then assume a source–time function of the form

$$V(x, t) = \frac{\Delta u(x)}{t_{\text{peak}}(x)} \left(\frac{t - t_{\text{rup}}(x)}{t_{\text{peak}}(x)} \right) \exp\left[-\left(\frac{t - t_{\text{rup}}(x)}{t_{\text{peak}}(x)} \right) \right],$$

for $t > t_{\text{rup}}(x)$

$V(x, t) = 0$, otherwise, $\qquad (15)$

in which $V(x, t)$ is the slip velocity as a function of time for each point along the fault profile, $\Delta u(x)$ is the final slip, and the peak time, $t_{\text{peak}}(x)$, is defined by

$$t_{\text{peak}}(x) = \frac{\Delta u(x)}{e V_{\text{peak}}(x)}. \qquad (16)$$
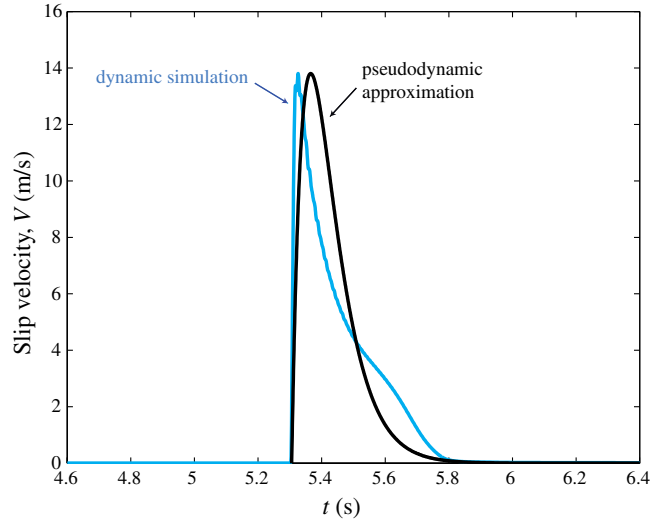
Figure 3. Source–time function for a point at position $x = 15$ km for the same typical dynamic simulation. Pseudodynamic approximation (equation 15) plotted for comparison. The color version of this figure is available only in the electronic edition.

$V(x, t)$ therefore satisfies the following relations:

$$\int_0^{\infty} V(x, t') \, dt' = \Delta u(x)$$
$$\max_t V(x, t) = V[x, t_{\text{peak}}(x)] = V_{\text{peak}}(x), \qquad (17)$$

and is thus fully constrained by our three source parameters. Source–time functions of this form have been used in previous kinematic models, such as the 2008 ShakeOut Scenario ground-motion simulation for California (Graves, Aagaard, and Hudnut, 2011), and generalize the exponential far-field source–time function derived by Brune (1970). This particular source–time function is consistent with slip velocities observed in our 2D dynamic ruptures for distances well away from the hypocenter (Fig. 3). Future iterations of the pseudodynamic models could incorporate alternative source–time functions, such as the Yoffe function (Yoffe, 1951), or its convolution with other windowing functions (Tinti *et al.*, 2005; Schmedes *et al.*, 2012).

Results

In the following section, we begin by comparing simulation results of the pseudodynamic rupture generator with those of fully dynamic simulations for a single realization of a nonplanar fault profile. Doing so allows for a direct and quantitative comparison of source parameters (as a function of position along the profile), and of the ground motion excited by each model type. We further compare these results with those of the same pseudodynamic model parameters projected onto planar fault. This permits us to examine the effect of the nonplanar fault geometry (i.e., the variability in local fault orientation) on the seismic wavefield, with the earthquake source parameters held fixed. This is an important factor to consider in seismic-hazard assessments (which
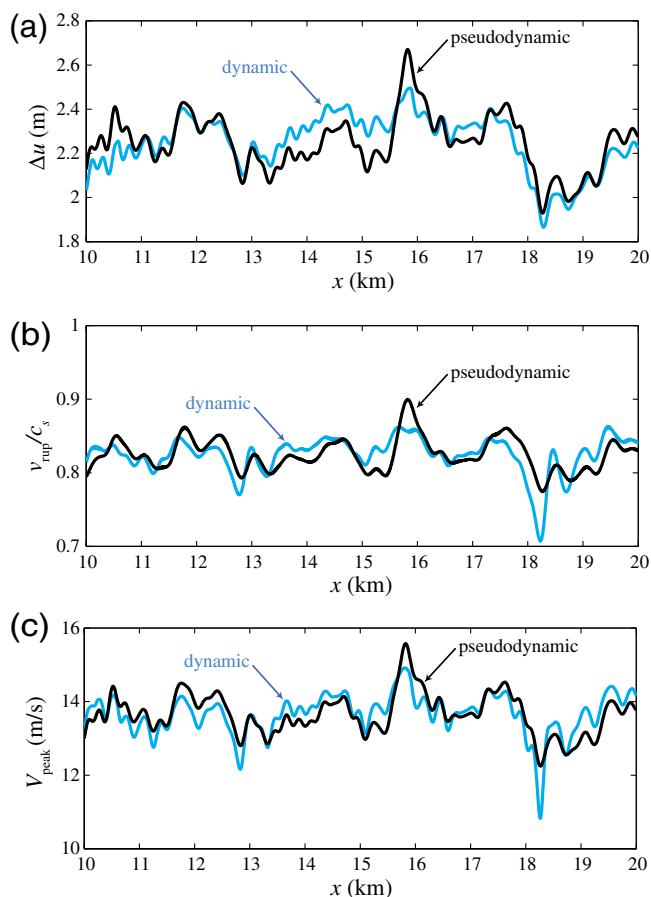
Figure 4. Comparison of source parameters in the region 10 km < x < 20 km for dynamic and pseudodynamic simulations on the same fault profile ($\alpha = 0.006$, $\tau_b = 38.5$ MPa, $\tau_b/\sigma_0 = 0.3056$). (a) Dynamic and pseudodynamic $\Delta u(x)$ (correlation coefficient 0.80). (b) Dynamic and pseudodynamic $v_{\mathrm{rup}}(x)$ (correlation coefficient 0.64). (c) Dynamic and pseudodynamic $V_{\mathrm{peak}}(x)$ (correlation coefficient 0.78). The color version of this figure is available only in the electronic edition.

typically use earthquake source models that assume planar fault geometry), because perturbations in fault orientation induce changes in seismic radiation patterns and thus may have a substantial influence on strong ground motion (Käser and Gallovic, 2008). Finally, we generalize this single-fault comparison to an ensemble analysis of dynamic and pseudodynamic models. The pseudodynamic simulations include off-fault plasticity to allow for a direct comparison with the dynamic simulations, though in both cases, the contribution to seismic moment from plastic strains is negligible. Additional details about the numerical method are discussed by Dunham *et al.* (2011a) and Kozdon *et al.* (2013).

Comparison of Pseudodynamic and Dynamic Models on a Single Fault Profile

Figure 4 plots the source parameters—$\Delta u(x)$, $v_{\mathrm{rup}}(x)$, and $V_{\mathrm{peak}}(x)$—for the three simulations in the region 10 km $\leq x \leq$ 20 km. The pseudodynamic source parameters
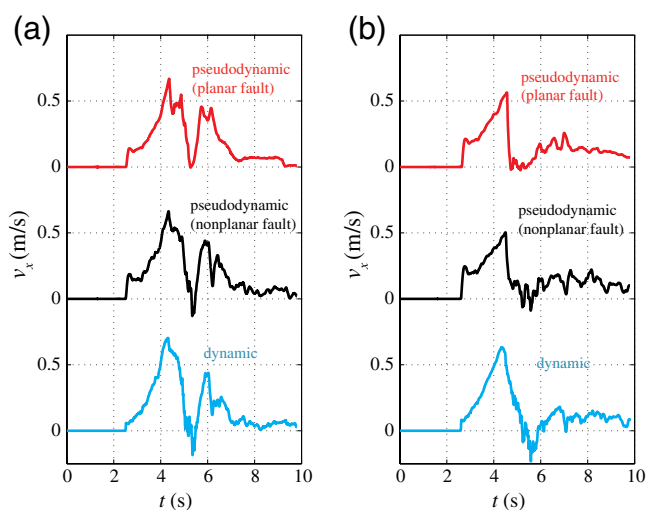
Figure 5. Fault-parallel velocity (v_x) seismograms at two stations for simulations using the same fault profile. Both stations are at $x = 15$ km, but different fault-normal distances. Simulation with the pseudodynamic source parameters projected onto a planar fault included for comparison (top). (a) Station 2 km off the fault. (b) Station 5 km off the fault. The color version of this figure is available only in the electronic edition.

closely match those generated by the fully dynamic rupture simulation. Both final slip $\Delta u(x)$ (Fig. 4a) and peak slip velocity $V_{\mathrm{peak}}(x)$ (Fig. 4c) are strongly correlated between the two models, with correlation coefficients of 0.80 and 0.78, respectively. The correlation of rupture velocity distributions, $v_{\mathrm{rup}}(x)$, is not quite as strong, with a correlation coefficient of 0.64. One explanation for this is that the dynamic rupture tends to experience long periods of stable propagation at nearly constant velocity, interspersed with brief but intense accelerations and decelerations (Dunham *et al.*, 2011b). The pseudodynamic model, however, is based only on the mean and standard deviations of rupture velocity observed in ensembles of dynamic models, and is thus more smoothly varying. These differences are further discussed in the Ensemble Comparison of Pseudodynamic and Dynamic Ruptures on Rough Faults section, in which we analyze the marginal distributions of ensembles of the pseudodynamic and dynamic models.

Given the highly correlated source parameter distributions of the two models, one might expect these similarities to carry over to the excitation of seismic ground motion. To test this claim, Figures 5 (fault-parallel velocity v_x) and 6 (fault-normal velocity v_y) show seismograms at stations 2 and 5 km from the local fault plane. Both stations are at a position of $x = 15$ km along strike, and the seismogram for the pseudodynamic model mapped onto a planar fault is included for the reference.

The three models generate largely similar ground motion at both stations. Notice that the fault-normal component (Fig. 6) produces substantially higher-amplitude ground motion than the fault-parallel component, as expected from the shear-wave radiation patterns for strike-slip rupture in this
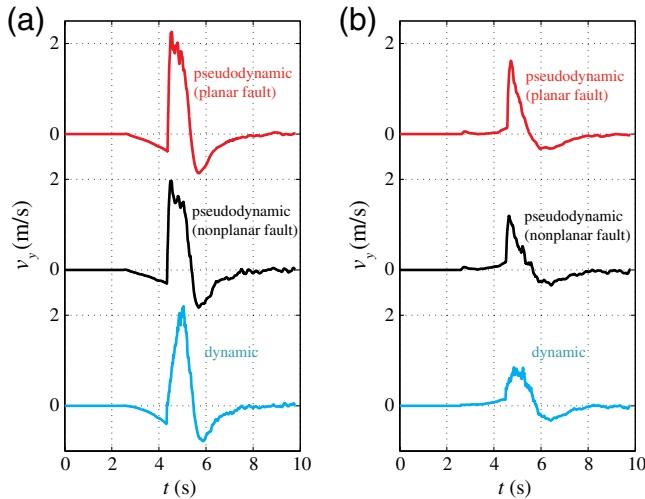
Figure 6. Fault-normal velocity (v_y) seismograms at two stations for simulations using the same fault profile. Both stations are at $x = 15$ km, but different fault-normal distances. Simulation with the pseudodynamic source parameters projected onto a planar fault included for comparison (top). (a) Station 2 km off the fault. (b) Station 5 km off the fault. The color version of this figure is available only in the electronic edition.

geometry (e.g., Aki and Richards, 2002). For the station nearer the fault profile (Fig. 6a), motion from near-field and intermediate-field P-wave causes $v_y(t)$ to become increasingly negative until the arrival of the S wave (Aki and Richards, 2002). Intense ground motion of positive polarity begins with this arrival of the hypocentral S wave, and increases in amplitude as the rupture front approaches. Fault-normal motion experiences a node as the rupture arrives, quickly becoming negative in polarity as the station moves into the opposite lobe of the S-wave radiation pattern. All three models have similar peak ground velocities (PGVs) of approximately 2 m/s at the closer station. This amplitude is reduced at the more distant station (Fig. 6b), with this increased source–receiver separation additionally serving to filter out the higher-frequency components of fault motion (Aki and Richards, 2002; Dunham and Archuleta, 2005).

Despite these similarities, it is important to note two subtle differences in the hypocentral arrivals of the three seismograms. These differences are best observed in the fault-parallel seismogram for the nearer station (Fig. 5a). Here the hypocentral P wave reaches the station at approximately $t = 2.5$ s. The first arrival of the dynamic model is very abrupt, creating an initial, high-frequency pulse of ground-motion acceleration. This sharp spike in acceleration is the result of the artificial nucleation procedure used to initiate the dynamic rupture. In contrast, the P-wave arrival for the pseudodynamic model is much more diffuse (i.e., the slope of the pulse is significantly lower). This is to be expected, as the pseudodynamic rupture does not require a transient shear-stress perturbation to initiate. This property of the pseudodynamic model is more representative of the natural earthquakes, which typically nucleate in response to progressive tectonic

loading (e.g., Ellsworth *et al.*, 1981; Kostrov and Das, 1988; Stein and Wysession, 2002) in critically stressed regions of the crust (Townend and Zoback, 2000). Furthermore, in our pseudodynamic model, slip initiates at single point and spreads out over a fault profile at the prescribed rupture velocity, consistent with the conclusion of Uchide and Ide (2007), among others, that earthquake nucleation is a self-similar process.

However, the overall amplitude of this initial pulse appears to be slightly larger for the pseudodynamic model. This discrepancy may be caused by the difference in shape of the source–time function for the two models. Near the hypocenter, the source–time function of the dynamic model consists of a sharp initial peak and a much broader tail, similar to a convolution of the Yoffe function described by Tinti *et al.* (2005). Thus, in the dynamic simulations, points near the hypocenter experience rapid initial slip followed by a slow decay in slip velocity after the nucleation pulse passes. This sequence is apparent in the seismogram of Figure 5a (bottom), in which a sharp initial acceleration is followed by a more gradual increase in particle velocity. In contrast, the pseudodynamic source–time function takes the form of equation (15) for all points along the fault profile, including those within the hypocentral region. Comparable slip occurs over a shorter overall time scale than in the dynamic simulations, producing a higher amplitude initial pulse in the seismogram.

We can obtain further insight into the ground-motion excitation of these models by viewing snapshots of the entire seismic wavefield. Figure 7 depicts the fault-normal particle velocity, v_y, at time $t = 4.9$ s, for each of the three simulations. At this time, the right-propagating rupture front has reached a position of $x \sim 14$ km along strike. Again, all three simulations capture the salient features of the seismic wavefield. Rupture directivity can be used to explain much of the observed features in the near-fault wavefield (Ripperger *et al.*, 2008). Strong ground motion is apparent in the stress lobes immediately in front of, and behind, the rupture front. The hypocentral S wave bounds the forward region of strong ground motion, whereas the negative polarity motion due to the near-field and intermediate-field P waves can be seen further along strike, and is bounded by the hypocentral P wave, which has nearly reached the right edge of the spatial domain.

Fault roughness has a substantial influence on the coherence of the wavefields. This effect can be most clearly seen by comparing Figure 7b and 7c, the rough and planar fault realizations of the pseudodynamic model. Although the planar realization has smoothly varying velocity fields, the superposition of adjacent radiation sources is more complex in the rough-fault realization, resulting in more regions of destructive interference. The wavefield in the fully dynamic simulation is quite similar to the rough-fault pseudodynamic simulation, though the increased duration of the dynamic source–time function results in a more diffuse wavefield. In particular, the strongest ground motion is more localized around the rupture front in the pseudodynamic simulations.

PGV and peak ground acceleration (PGA) are scalar measures that can help to quantify these differences, and are also
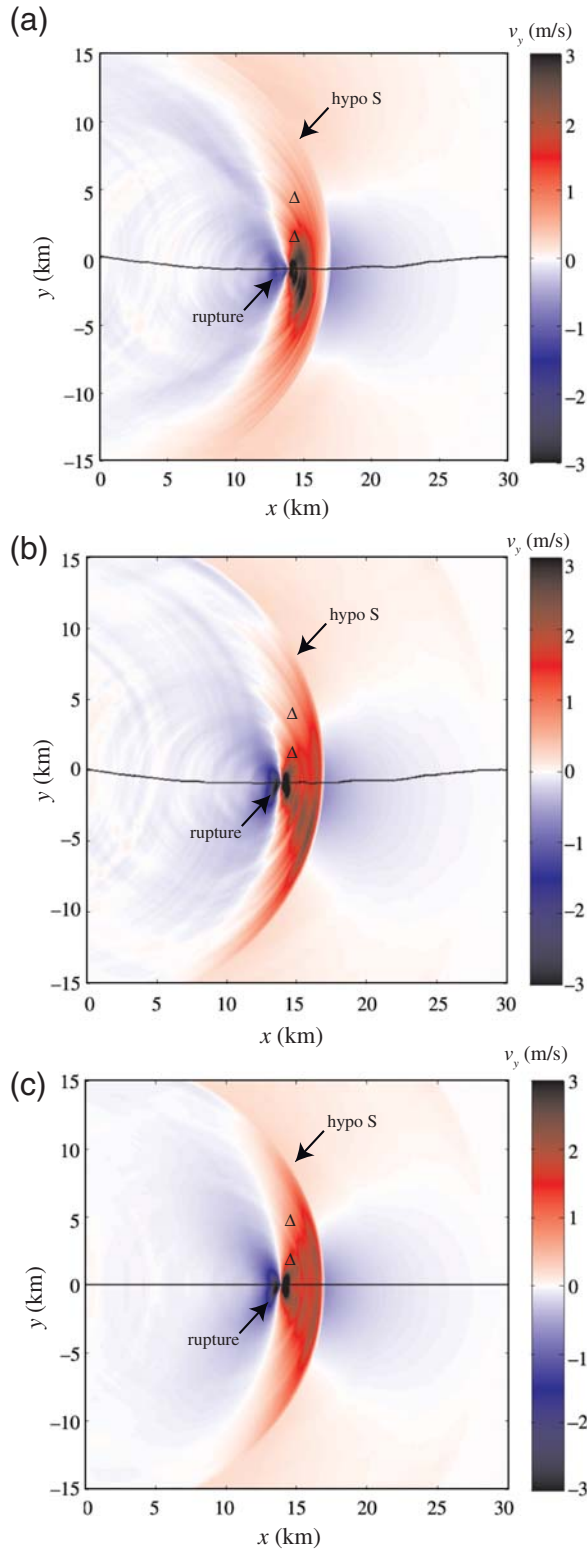
(a)

(b)

(c)

Figure 7. Snapshot at $t = 4.9$ s of the fault-normal velocity field (v_y) for the same sets of simulations as in Figures 4–6. The rupture front and hypocentral S-wave front are marked. The two stations at which the seismograms of Figures 5 and 6 are calculated are marked with triangles. (a) Dynamic simulation. (b) Pseudodynamic simulation on the nonplanar fault. (c) Pseudodynamic simulation with the same source parameters, but on a planar fault. The color version of this figure is available only in the electronic edition.

(a)

(b)
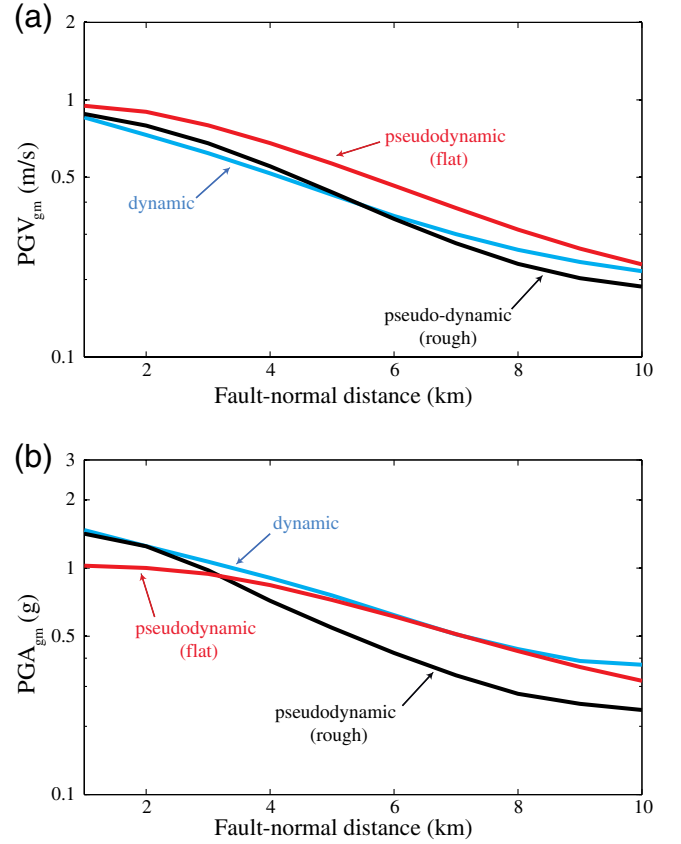
Figure 8. Peak ground motion as a function of fault-normal distance for the same set of simulations as in Figures 4–7. (a) Geometric mean of peak ground velocity (PGV$_{gm}$), averaged over a grid of 100 stations (1 km grid spacing). (b) Geometric mean of peak ground acceleration (PGA$_{gm}$), averaged over a grid of 100 stations (1 km grid spacing). The color version of this figure is available only in the electronic edition.

commonly used to assess seismic hazard (e.g., Boore and Atkinson, 2008; Douglas and Aochi, 2008; O'Connell *et al.*, 2012). To this end, Figure 8a plots the geometric mean of the *x*- and *y*-component PGV

$$
\text{PGV}_{gm} = \exp\left[\frac{\log(\text{PGV}_x) + \log(\text{PGV}_y)}{2}\right]
$$
$$
= \sqrt{(\text{PGV}_x)(\text{PGV}_y)}, \tag{18}
$$

as a function of fault-normal distance. All three simulations exhibit comparable values for the decay of PGV$_{gm}$ with distance. The planar-fault realization of the pseudodynamic model exhibits the strongest ground motion. PGV$_{gm}$ for the rough-fault pseudodynamic model is nearly identical to that of the dynamic model, with slightly stronger motion near the fault and slightly weaker motion away from the fault. These general trends reinforce our observations of the seismic wavefield (Fig. 7).

Interestingly, the geometric-mean PGA, PGA$_{gm}$ (Fig. 8b), is slightly higher for stations nearer the fault profile in both the dynamic and the rough-fault pseudodynamic simulation
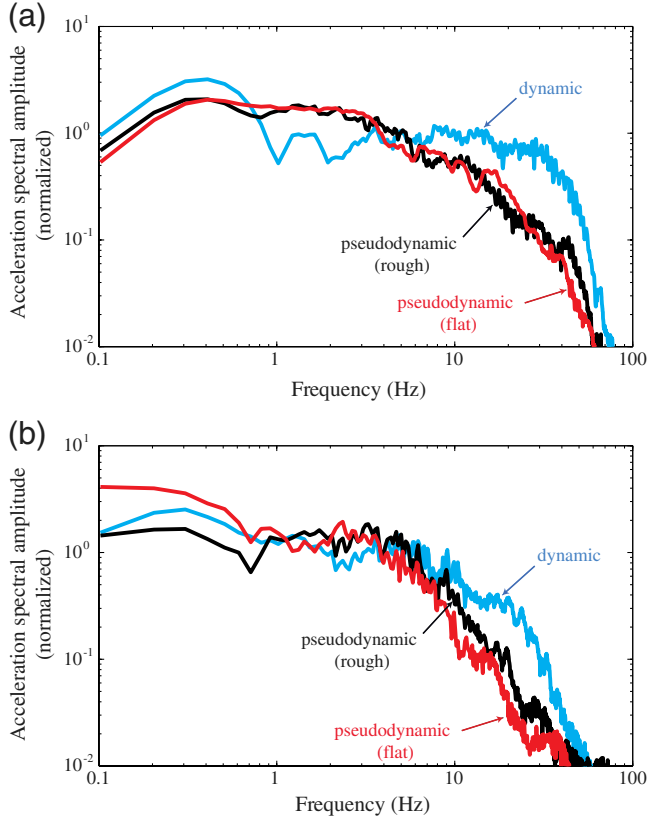
Figure 9. Fourier amplitude spectrum (FAS) for the fault-normal component of acceleration (a_y) for the same set of simulations as Figures 4–8. Individual Fourier spectra are normalized to unit amplitude between 0 and 10 Hz before averaging over a grid of 10 stations (1 km grid spacing). All stations are at a fault normal distance of 5 km. (a) FAS for complete seismogram, including hypocentral *S*-wave nucleation arrival. (b) FAS for seismograms windowed to exclude the hypocentral *S*-wave nucleation arrival. The color version of this figure is available only in the electronic edition.

than it is for the planar-fault pseudodynamic simulation. Geometric irregularities in the fault profile and rupture directivity effects for the rough-fault simulations generate high-frequency seismic radiation (Dunham *et al.*, 2011b). This tends to elevate levels of $\mathrm{PGA_{gm}}$ for stations nearer the fault, but these bursts of waves from localized regions quickly lose amplitude due to geometrical spreading. The same general trend can be observed by comparing the two pseudodynamic model realizations in Figure 8a, as the disparity in $\mathrm{PGV_{gm}}$ is smaller nearer the fault.

To better quantify the frequency content of the seismic wavefield, we compute the Fourier amplitude spectra (FAS) of the fault-normal acceleration averaged over stations at a fault-normal distance of 5 km (Shi and Day, 2013). The fault-normal acceleration FAS, $\hat{A}_y(f)$, is defined by

$$\hat{A}_y(f) = \|\hat{a}_y(f)\|, \tag{19}$$

in which $\|\hat{a}_y(f)\|$ refers to the amplitude of the Fourier transform of the fault-normal acceleration $a_y(t)$. To facilitate spatial averaging, we normalize to mean unit amplitude between

0 and 10 Hz. Figure 9a shows the FAS of $a_y(t)$ for the complete duration of the seismogram, whereas Figure 9b windows each seismogram to remove the hypocentral first arrival. For the complete seismogram, the high-frequency content is amplified by the overly sharp hypocentral *S*-wave arrival, a product of the artificial nucleation. When windowed to remove this factor (Fig. 9b), the amplitude spectrum is more representative of the rupture process as a whole, excluding nucleation, and therefore allows for a more useful comparison between the frequency content of the dynamic and pseudodynamic ruptures. Because the roughness on our nonplanar fault profile has minimum wavelength $\lambda_{\min} = 0.3$ km, we expect seismic-wave excitation to fall off at a characteristic frequency $\sim c_s / \lambda_{\min} \sim 10$ Hz (Dunham *et al.*, 2011b).

More crucially, both the rough-fault pseudodynamic model and the dynamic model have a relatively flat frequency spectrum (up to frequencies of $\sim c_s / \lambda_{\min}$) consistent with strong-motion records (Andrews, 1981; Hanks and McGuire, 1981). It is important to note, however, that the dynamic model is enriched in high-frequency energy relative to the pseudodynamic model. As discussed in the Ensemble Comparison of Pseudodynamic and Dynamic Ruptures on Rough Faults section, this may be due to the tendency for dynamic ruptures to propagate at nearly constant speed, interspersed with short but intense periods of rupture acceleration and deceleration. The planar-fault realization is deficient in high-frequency radiation, as expected from its more coherent wavefield.

Ensemble Comparison of Pseudodynamic and Dynamic Ruptures on Rough Faults

In the previous subsection, Comparison of Pseudodynamic and Dynamic Models on a Single Fault Profile, we compared the ground motion for a pseudodynamic and dynamic model specific to a single fault profile. To test whether these observations generalize, we compare the averages over ensembles of 30 pseudodynamic and 30 dynamic rupture simulations, both of which were implemented on rough faults. The dynamic simulations are themselves distinct from the ensemble used to synthesize our pseudodynamic rupture generator.

We begin by comparing the marginal distributions for the final slip, $\Delta u(x)$. Figure 10a shows relative-frequency histograms for ensembles of each model type. The mean and standard deviations of the two distributions are similar: 1.95 ± 0.34 m for the dynamic model and 1.96 ± 0.32 m for the pseudodynamic model. The pseudodynamic distribution is Gaussian in shape, as prescribed by our model assumptions. The dynamic distribution is also approximated well by a Gaussian distribution, though it is slightly broader, and less sharply peaked.

Unlike those for $\Delta u(x)$, the marginal distributions for rupture velocity, $v_{\mathrm{rup}}(x)$ is noticeably different in shape. Relative-frequency histograms for v_{rup}/c_s are shown in Figure 10b. Again, the mean and standard deviations of the normalized distributions are similar: $0.83 \pm 0.035\ c_s$ for the
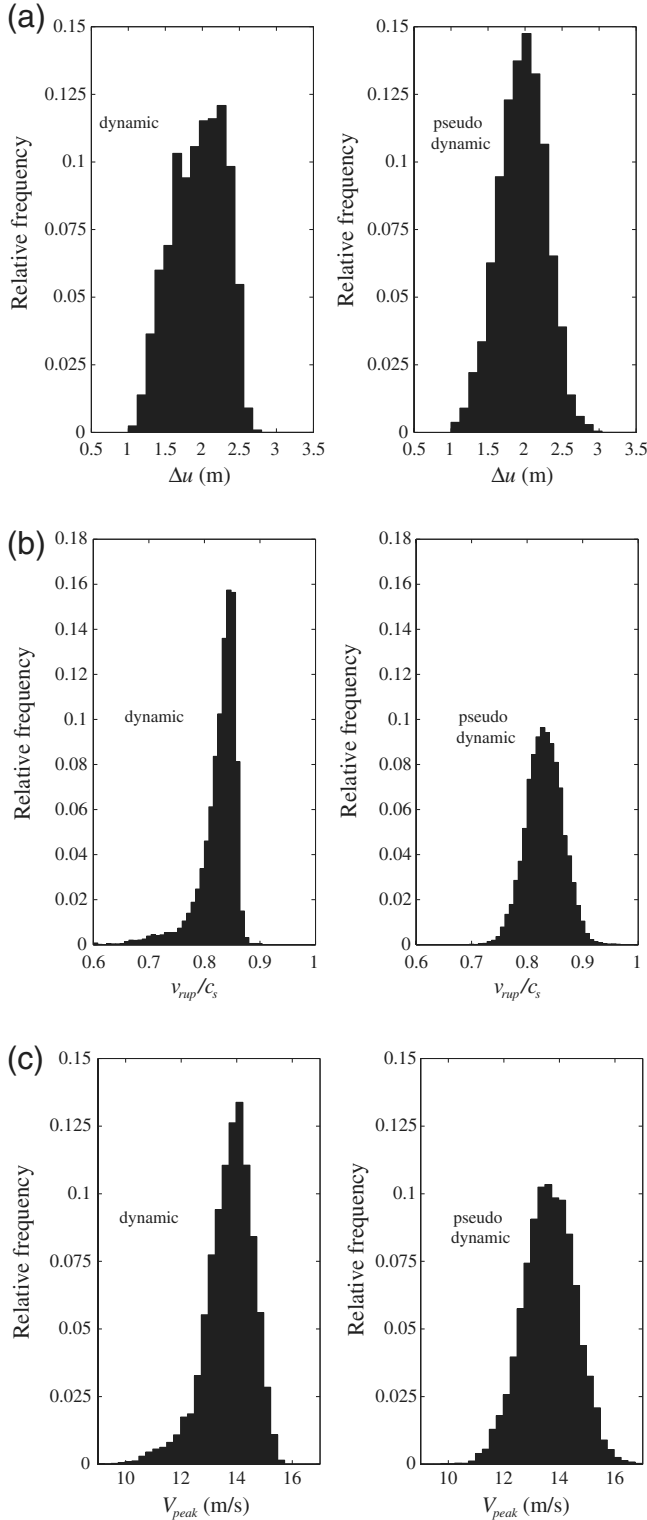
Figure 10.   Relative frequency histograms showing marginal distribution of source parameters for ensembles of dynamic simulations (left) and pseudodynamic simulations (right) Each simulation is implemented along a different nonplanar fault profile ($\alpha = 0.006$, $\tau_b = 38.5$ MPa, and $\tau_b/\sigma_0 = 0.3056$). Only points in the region 10 km $< |x| <$ 20 km are included in the histograms. Comparison of ensemble marginal distributions for (a) final slip, Δu, (b) rupture velocity normalized by shear-wave speed, v_{rup}/c_s, and (c) peak slip velocity, V_{peak}.

dynamic model and 0.83 ± 0.033 c_s for the pseudodynamic model. The dynamic model, however, is distinctly non-Gaussian. It is strongly skewed toward lower-rupture velocities, with a sharper peak at the mode of the distribution. The more pronounced mode in the dynamic simulations' marginal distribution demonstrates the tendency for dynamic ruptures to propagate at near-constant velocity for much of their duration. Meanwhile, the large accelerations associated with the transition from velocities in the modal and tail parts of the dynamic distribution generate extra high-frequency radiation (Madariaga, 1977), which is not observed in the pseudodynamic model. Although rupture velocity is strongly anticorrelated with fault slope in both models, the dynamic rupture reacts in a nonlinear way to such geometrical perturbations, an effect not captured by a simple correlation coefficient.

$V_{\mathrm{peak}}(x)$ also deviates from a Gaussian distribution for the dynamic model, though not as severely as does $v_{\mathrm{rup}}(x)$. Once again, the mean and standard deviations of the dynamic and pseudodynamic distributions are comparable, with values of 13.7 ± 0.9 and 13.6 ± 0.9 m/s, respectively. The marginal distribution for the dynamic model is slightly skewed toward lower-peak slip velocities (Fig. 10c). This result is somewhat surprising, given the symmetry of the $\Delta u(x)$ distribution, but can be explained in terms of the marginal distribution of rise time. In our dynamic rupture simulations, the rise time distribution is not quite Gaussian, but is instead slightly skewed toward longer rise times. In contrast, the rise time marginal distribution for pseudodynamic model is Gaussian, given the assumed source–time function (equation 15).

Ensemble averages of the PGV$_{\mathrm{gm}}$ and PGA$_{\mathrm{gm}}$ are consistent with the trends observed in the direct comparisons for the single fault profile. PGV$_{\mathrm{gm}}$ values are similar in magnitude for both models, though slightly higher for the pseudodynamic model for stations near the fault profile (Fig. 11a). This is to be expected, as its velocity field is more coherent near the rupture front (Fig. 7b). PGA$_{\mathrm{gm}}$ values near the fault are almost identical for both models, though are slightly reduced in the pseudodynamic model further from the fault (Fig. 11b). As can be determined from the wavefields for the dynamic simulations (e.g., Fig. 7a), artificial rupture nucleation creates more intense hypocentral waves than are present in the pseudodynamic simulations (e.g., Fig. 7b). At stations well away from the profile (and hence from the rupture front), the hypocentral shear wavefront is the dominant contribution to ground-motion acceleration, creating larger PGA$_{\mathrm{gm}}$ values in the dynamic simulations.

To compare the frequency content of the seismic wavefield for the two ensembles, we again compute the Fourier amplitude spectrum of the fault-normal acceleration (Fig. 12). As in the previous subsection, Comparison of Pseudodynamic and Dynamic Models on a Single Fault Profile, we average over stations at a fault-normal distance of 5 km, and normalize to mean unit amplitude in the frequency band < 10 Hz. In Figure 12b, seismograms have been windowed to remove the ground motion caused by nucleation. The ensemble averages are consistent with the results highlighted in
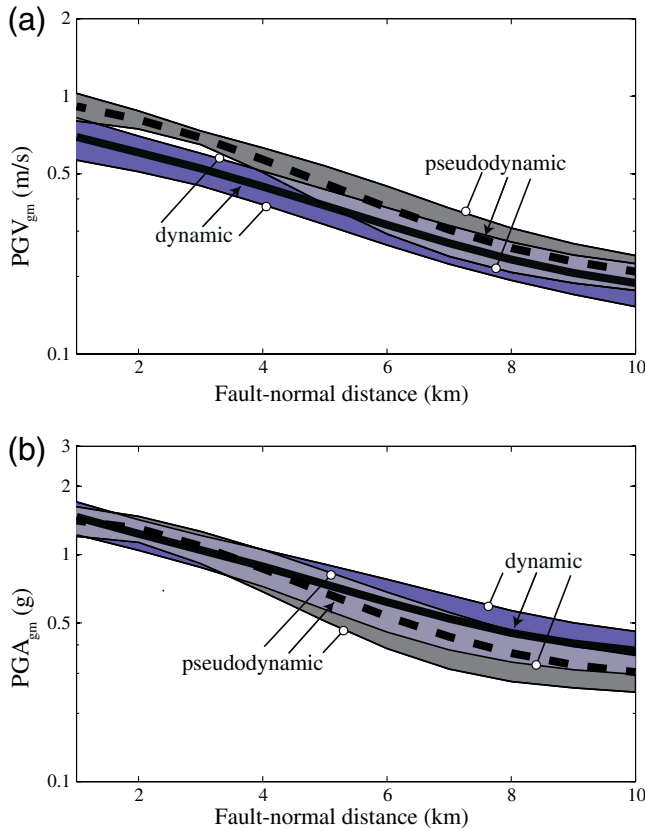
Figure 11. Peak ground motion as a function of fault-normal distance for ensembles of 30 dynamic and 30 pseudodynamic simulations. Ensemble mean values are displayed as thick lines (marked with arrows), with the solid line denoting the dynamic simulation mean and the dashed line denoting the pseudodynamic simulation mean. Mean values plus and minus one standard deviation are displayed as thin lines (marked with circles). (a) Geometric mean of peak ground velocity (PGV$_{gm}$), averaged over a grid of 100 stations per simulation (1 km grid spacing). (b) Geometric mean of peak ground acceleration (PGA$_{gm}$), averaged over a grid of 100 stations per simulation (1 km grid spacing). The color version of this figure is available only in the electronic edition.

Figure 12. Ensemble averages of Fourier amplitude spectra (FAS) for the fault-normal component of acceleration (a_y). For each simulation in the ensemble, individual Fourier spectra are normalized to unit amplitude between 0 and 10 Hz before averaging over a grid of 10 stations (1 km grid spacing). All stations are at a fault normal distance of 5 km. (a) FAS for the complete seismogram, including the hypocentral S-wave nucleation arrival. (b) FAS for seismograms windowed to exclude the hypocentral S-wave nucleation arrival. The color version of this figure is available only in the electronic edition.

the previous subsection. Both models have flat frequency spectra up to frequencies of $\sim c_s / \lambda_{\min} \sim 10$ Hz. The dynamic ensemble has a greater high-frequency component due to abrupt accelerations and decelerations of the rupture front.

Discussion

Motivated by observations of 2D dynamic rupture simulations on fractally rough faults, we have developed a preliminary pseudodynamic rupture generator that incorporates a spatial dependence of earthquake source parameters on local fault geometry. We model three scalar source parameters—final slip Δu, local rupture velocity v_{rup}, and peak slip velocity V_{peak}—as spatial random fields with Gaussian marginal distributions and exponential autocorrelation functions. These fields are anticorrelated with local fault slope, suppressing slip and rupture velocity in compressional regions while elevating them in extensional regions. We complete the

pseudodynamic model by fitting these three source parameters to an exponential source–time function of the form given by equation (15). Pseudodynamic models synthesized in this way can be used to compute ground motion at a considerable computational savings compared with dynamic rupture simulations. Furthermore, because the pattern of stress heterogeneity in our pseudodynamic ruptures is based on fault roughness, which is directly observable, our model eliminates an important source of epistemic uncertainty present in the previous pseudodynamic models.

Our pseudodynamic model captures the key characteristics of the seismic wavefield observed in dynamic simulations. Averaged over ensembles of pseudodynamic and dynamic simulations, we find that the two models produce comparable predictions for PGV and PGA as a function of fault-normal distance. Short-wavelength fluctuations in model source parameters produce flat acceleration spectra out to frequencies ~ 10 Hz, an essential feature to replicate for the purposes of seismic-hazard analysis. The model even

provides one specific improvement over our dynamic simulations, in that the pseudodynamic model does not generate the sharp hypocentral wavefront associated with the artificial nucleation of our dynamic ruptures.

These promising results indicate that fault roughness is a key factor to consider in using earthquake simulations to assess seismic hazard. In practice, one could approximate nonplanarity in the fault interface while still using the existing codes for computing seismic hazard on planar faults by allowing for different moment tensor orientations at each point on the planar fault interface. Although our pseudodynamic model is an important first step in an effort to incorporate geometric complexity of the fault interface into seismic-hazard analysis, a number of improvements could be made to future model iterations. First, we represent the source parameters as spatial random fields that have Gaussian marginal distributions and exponential autocorrelation functions. Our selection of Gaussian marginals reflected our epistemic uncertainty in the true nature of these distributions. In the case of final slip Δu, dynamic simulations appear to support this choice. The same cannot be said for rupture velocity v_{rup}, in which our dynamic models have sharply peaked distributions, which are skewed toward lower-rupture velocities (Fig. 10b). Data from real earthquakes, such as the 1994 Northridge earthquake, reinforce these observations (Ma and Archuleta, 2006). Furthermore, as demonstrated by Mena et al. (2012), among others, supershear rupture velocities are pervasive in asperity-model dynamic rupture simulations of large earthquakes, and presumably, in the earth itself. Hence, a bimodal marginal distribution with peaks at both subshear and supershear velocities, may be the most appropriate choice for rupture velocity.

Further research could be directed toward establishing best-fitting marginal distributions for dynamic simulations, and cross referencing these with field data for consistency. Once a parameter distribution is chosen, the procedure used to synthesize our pseudodynamic model could easily be generalized to non-Gaussian marginal distributions through a normal-score transform (Cario and Nelson, 1997; Liu et al., 2006; Song and Dalguer, 2013). Similar modifications could be made to the form of the source–time function and to parameter autocorrelations.

Our pseudodynamic model also assumes stationary marginal distributions in the sense that these distributions are independent of distance from the hypocenter. Dynamic rupture simulations do not strictly obey these assumptions, as evidenced by the prominent peak in slip near the hypocenter (e.g., Fig. 1c). However, this feature is a product of the artificial nucleation process required to initiate our dynamic ruptures, and is hence not desirable to replicate in a pseudodynamic model. Mai et al. (2005) observed that, for natural earthquakes, hypocenters tend to be located near a region of large slip. This is an intrinsic feature of our pseudodynamic model, as we choose the hypocenter to be the location of maximal smoothed τ/σ, a region with local fault geometry that favors large slip.

Schmedes et al. (2012) also found that the marginal distributions for source parameters in dynamic rupture simulations are dependent on hypocentral distance. They chose to incorporate this feature into their rupture model by implementing different marginal distributions for each of several distance bins. An analogous approach could be used to modify our pseudodynamic model, and perhaps extended to apply different forms of the source–time function to different sections of the fault profile. In contrast, Wesnousky (2008) did not find any systematic correlation of the hypocenter position and the region of maximal slip in his study of real earthquakes. It is therefore possible that stationary parameter distributions may better characterize the natural behavior of earthquakes.

Finally, we note that our dynamic simulations, and hence our pseudodynamic model, are implemented in 2D. The 2D problem is computationally much simpler and provides a reasonable approximation for certain rupture geometries (like the strike-slip orientation studied here). There are, nonetheless, fundamental differences between the study of earthquakes in 2D and 3D. These range from different amplitude factors governing the geometrical spreading of seismic waves, to an expected increase in ground-motion incoherence in 3D due to fault roughness in the out-of-plane direction (Dunham et al., 2011b). Shi and Day (2013) have recently performed the first 3D dynamic rupture simulations on fractal faults, verifying the strong interrelation between fault roughness and earthquake source parameters. Such simulations, although requiring enormous computational power, will undoubtedly give deeper insight into earthquake rupture mechanics and the excitation of seismic waves. This newfound knowledge could be leveraged to create more physically realistic pseudodynamic source models and greatly improve our ability to quantify seismic hazard.

Data and Resources

Numerical simulations were conducted at the Stanford Center for Computational Earth and Environmental Science (CEES).

Acknowledgments

References

Abrahamson, N., and W. Silva (2008). Summary of the Abrahamson & Silva NGA ground-motion relations, *Earthq. Spectra* **24,** no. 1, 67–97, doi: 10.1193/1.2924360.

Aki, K., and P. Richards (2002). *Quantitative Seismology*, University Science Books, Sausalito, California, 700 pp.

Anderson, J. G., and J. N. Brune (1999). Probabilistic seismic hazard analysis without the ergodic assumption, *Seismol. Res. Lett.* **70,** no. 1, 19–28, doi: 10.1785/gssrl.70.1.19.

Andrews, D. J. (1976). Rupture velocity of plane strain shear cracks, *J. Geophys. Res.* **81,** no. 32, 5679–5687, doi: 10.1029/JB081i032p05679.

Andrews, D. J. (1980). A stochastic fault model, 1. Static case, *J. Geophys. Res.* **85,** no. NB7, 3867–3877, doi: 10.1029/JB085iB07p03867.

Andrews, D. J. (1981). A stochastic fault model, 2. Time-dependent case, *J. Geophys. Res.* **86,** no. B11, 10,821–10,834, doi: 10.1029/JB086iB11p10821.

Beeler, N. M., T. E. Tullis, and D. L. Goldsby (2008). Constitutive relationships and physical basis of fault strength due to flash heating, *J. Geophys. Res.* **113,** no. B1, B01401, doi: 10.1029/2007JB004988.

Boore, D. M. (2003). Simulation of ground motion using the stochastic method, *Pure Appl. Geophys.* **160,** 635–676.

Boore, D. M., and G. M. Atkinson (2008). Ground-motion prediction equations for the average horizontal component of PGA, PGV, and 5%-damped PSA at spectral periods between 0.01 s and 10.0 s, *Earthq. Spectra* **24,** no. 1, doi: 10.1193/1.2830434.

Brown, S. R., and C. H. Scholz (1985). Broad bandwidth study of the topography of natural rock surfaces, *J. Geophys. Res.* **90,** no. B14, 12,575–12,582, doi: 10.1029/JB090iB14p12575.

Brune, J. N. (1970). Tectonic stress and the spectra of seismic shear waves from earthquakes, *J. Geophys. Res.* **75,** no. 26, 4997–5009, doi: 10.1029/JB075i026p04997.

Candela, T., F. Renard, Y. Klinger, K. Mair, J. Schmittbuhl, and E. E. Brodsky (2012). Roughness of fault surfaces over nine decades of length scales, *J. Geophys. Res.* **117,** no. B8, B08409, doi: 10.1029/2011JB009041.

Cario, M. C., and B. L. Nelson (1997). Modeling and generating random vectors with arbitrary marginal distributions and correlation matrix, Technical Report, Department of Industrial Engineering and Management Sciences, Northwestern University, Evanston, Illinois.

Christakos, G. (1992). *Random Field Models in Earth Sciences*, Academic Press Inc., San Diego, California, 512 pp.

Das, S., and K. Aki (1977). Fault plane with barriers: A versatile earthquake model, *J. Geophys. Res.* **82,** no. 36, 5658–5670, doi: 10.1029/JB082i036p05658.

Day, S. M. (1982). Three-dimensional finite difference simulation of fault dynamics: Rectangular faults with fixed rupture velocity, *Bull. Seismol. Soc. Am.* **72,** 705–727.

Di Toro, G., D. L. Goldsby, and T. E. Tullis (2004). Friction falls towards zero in quartz rock as slip velocity approaches seismic rates, *Nature* **427,** no. 6973, 436–439, doi: 10.1038/nature02249.

Dieterich, J. H. (1992). Earthquake nucleation on faults with rate-and state-dependent strength, *Tectonophysics* **211,** nos. 1–4, 115–134, doi: 10.1016/0040-1951(92)90055-B.

Douglas, J., and H. Aochi (2008). A survey of techniques for predicting earthquake ground motions for engineering purposes, *Surv. Geophys.* **29,** no. 3, 187–220, doi: 10.1007/s10712-008-9046-y.

Dunham, E. M. (2007). Conditions governing the occurrence of supershear ruptures under slip-weakening friction, *J. Geophys. Res.* **112,** no. B7, B07302, doi: 10.1029/2006JB004717.

Dunham, E. M., and R. J. Archuleta (2005). Near-source ground motion from steady state dynamic rupture pulses, *Geophys. Res. Lett.* **32,** no. 3, L03302, doi: 10.1029/2004GL021793.

Dunham, E. M., D. Belanger, L. Cong, and J. E. Kozdon (2011a). Earthquake ruptures with strongly rate-weakening friction and off-fault plasticity, part 1: Planar faults, *Bull. Seismol. Soc. Am.* **101,** no. 5, 2296–2307, doi: 10.1785/0120100075.

Dunham, E. M., D. Belanger, L. Cong, and J. E. Kozdon (2011b). Earthquake ruptures with strongly rate-weakening friction and off-fault plasticity, Part 2: Nonplanar faults, *Bull. Seismol. Soc. Am.* **101,** no. 5, 2308–2322, doi: 10.1785/0120100076.

Ellsworth, W., A. Lindh, W. Prescott, and D. Herd (1981). The 1906 San Francisco earthquake and the seismic cycle, in *Earthquake Prediction: An International Review*, D. W. Simpson and P. G. Richards (Editors), Vol. 4, 126–140.

Fang, Z., and E. M. Dunham (2013). Additional shear resistance from fault roughness and stress levels on geometrically complex faults, *J. Geophys. Res.* **118,** no. 7, 3642–3654, doi: 10.1002/jgrb.50262.

Freund, L. B. (1990). *Dynamic Fracture Mechanics*, Cambridge University Press, Cambridge, United Kingdom, 563 pp.

Fukuyama, E., and R. Madariaga (1998). Rupture dynamics of a planar fault in a 3D elastic medium: Rate- and slip-weakening friction, *Bull. Seismol. Soc. Am.* **88,** no. 1, 1–17.

Gabriel, A.-A., J.-P. Ampuero, L. A. Dalguer, and P. M. Mai (2012). The transition of dynamic rupture styles in elastic media under velocity-weakening friction, *J. Geophys. Res.* **117,** B09311, doi: 10.1029/2012JB009468.

Graves, R. W., B. T. Aagaard, and K. W. Hudnut (2011). The ShakeOut earthquake source and ground motion simulations, *Earthq. Spectra* **27,** no. 2, 273–291, doi: 10.1193/1.3570677.

Graves, R. W., T. H. Jordan, S. Callaghan, E. Deelman, E. Field, G. Juve, C. Kesselman, P. Maechling, G. Mehta, and K. Milner (2011). Cyber-Shake: A physics-based seismic hazard model for southern California, *Pure Appl. Geophys.* **168,** nos. 3–4, 367–381, doi: 10.1007/s00024-010-0161-6.

Guatteri, M., P. M. Mai, and G. Beroza (2004). A pseudo-dynamic approximation to dynamic rupture models for strong ground motion prediction, *Bull. Seismol. Soc. Am.* **94,** no. 6, 2051–2063, doi: 10.1785/0120040037.

Guatteri, M., P. M. Mai, G. C. Beroza, and J. Boatwright (2003). Strong ground-motion prediction from stochastic-dynamic source models, *Bull. Seismol. Soc. Am.* **93,** no. 1, 301–313, doi: 10.1785/0120020006.

Hanks, T. C., and R. K. McGuire (1981). The character of high-frequency strong ground motion, *Bull. Seismol. Soc. Am.* **71,** no. 6, 2071–2095.

Haskell, N. A. (1966). Total energy and energy spectral density of elastic wave radiation from propagating faults. Part II. A statistical source model, *Bull. Seismol. Soc. Am.* **56,** no. 1, 125–140.

Herrero, A., and P. Bernard (1994). A kinematic self-similar rupture process for earthquakes, *Bull. Seismol. Soc. Am.* **84,** 1216–1228.

Hutchings, L. (1994). Kinematic earthquake models and synthesized ground motion using empirical Greens-functions, *Bull. Seismol. Soc. Am.* **84,** no. 4, 1028–1050.

Käser, M., and F. Gallovic (2008). Effects of complicated 3-D rupture geometries on earthquake ground motion and their implications: a numerical study, *Geophys. J. Int.* **172,** no. 1, 276–292, doi: 10.1111/j.1365-246X.2007.03627.x.

Kostrov, B. V., and S. Das (1988). *Principles of Earthquake Source Mechanics*, Cambridge University Press, Cambridge, 286 pp.

Kozdon, J. E., E. M. Dunham, and J. Nordström (2013). Simulation of dynamic earthquake ruptures in complex geometries using high-order finite difference methods, *J. Sci. Comput.* **55,** no. 1, 92–124, doi: 10.1007/s10915-012-9624-5.

Lavallée, D., P. Liu, and R. J. Archuleta (2006). Stochastic model of heterogeneity in earthquake slip spatial distributions, *Geophys. J. Int.* **165,** no. 2, 622–640, doi: 10.1111/j.1365-246X.2006.02943.x.

Lee, J.-J., and R. L. Bruhn (1996). Structural anisotropy of normal fault surfaces, *J. Struct. Geol.* **18,** no. 8, 1043–1059, doi: 10.1016/0191-8141(96)00022-3.

Liu, P., R. J. Archuleta, and S. H. Hartzell (2006). Prediction of broadband ground-motion time histories: Hybrid low/high-frequency method with correlated random source parameters, *Bull. Seismol. Soc. Am.* **96,** no. 6, 2118–2130, doi: 10.1785/0120060036.

Liu, Y., and N. Lapusta (2008). Transition of mode II cracks from sub-Rayleigh to intersonic speeds in the presence of favorable heterogeneity, *J. Mech. Phys. Solids* **56,** no. 1, 25–50, doi: 10.1016/j.jmps.2007.06.005.

Ma, S., and R. J. Archuleta (2006). Radiated seismic energy based on dynamic rupture models of faulting, *J. Geophys. Res.* **111,** B05315, doi: 10.1029/2005JB004055.

Madariaga, R. (1977). High-frequency radiation from crack (stress drop) models of earthquake faulting, *Geophys. J. Roy. Astron. Soc.* **51,** no. 3, 625–651, doi: 10.1111/j.1365-246X.1977.tb04211.x.

Madariaga, R. (2007). Seismic Source Theory, in *Treatise on Geophysics*, G. Schubert (Editor), Elsevier, Amsterdam, the Netherlands, 59–81.

Mai, P. M., and G. Beroza (2002). A spatial random field model to characterize complexity in earthquake slip, *J. Geophys. Res.* **107,** no. B11, 2308, doi: 10.1029/2001JB000588.

Mai, P. M., P. Spudich, and J. Boatwright (2005). Hypocenter locations in finite-source rupture models, *Bull. Seismol. Soc. Am.* **95,** no. 3, 965–980, doi: 10.1785/0120040111.

Mena, B., L. A. Dalguer, and P. M. Mai (2012). Pseudodynamic source characterization for strike-slip faulting including stress heterogeneity and super-shear ruptures, *Bull. Seismol. Soc. Am.* **102,** no. 4, 1654–1680, doi: 10.1785/0120110111.

O'Connell, D., J. Ake, F. Bonilla, P. Liu, R. LaForge, and D. Ostenaa (2012). Strong ground motion estimation, in *Earthquake Research and Analysis—New Frontiers in Seismology*, S. D'Amico (Editor), Intech Publishing, Rijeka, Croatia, 3–68.

Oglesby, D. D., and S. M. Day (2002). Stochastic fault stress: Implications for fault dynamics and ground motion, *Bull. Seismol. Soc. Am.* **92,** no. 8, 3006–3021, doi: 10.1785/0120010249.

Oglesby, D. D., P. M. Mai, K. Atakan, and S. Pucci (2008). Dynamic models of earthquakes on the North Anatolian fault zone under the Sea of Marmara: Effect of hypocenter location, *Geophys. Res. Lett.* **35,** no. 18, L18302, doi: 10.1029/2008GL035037.

Power, W. L., and T. E. Tullis (1991). Euclidean and fractal models for the description of rock surface roughness, *J. Geophys. Res.* **96,** no. B1, 415–424, doi: 10.1029/90JB02107.

Ripperger, J., J. P. Ampuero, P. M. Mai, and D. Giardini (2007). Earthquake source characteristics from dynamic rupture with constrained stochastic fault stress, *J. Geophys. Res.* **112,** no. B04311, doi: 10.1029/2006JB004515.

Ripperger, J., P. M. Mai, and J. P. Ampuero (2008). Variability of near-field ground motion from dynamic earthquake rupture simulations, *Bull. Seismol. Soc. Am.* **98,** no. 3, 1207–1228, doi: 10.1785/0120070076.

Sagy, A., and E. E. Brodsky (2009). Geometric and rheological asperities in an exposed fault zone, *J. Geophys. Res.* **114,** no. B2, B02301, doi: 10.1029/2008JB005701.

Schmedes, J., R. J. Archuleta, and D. Lavallée (2010). Correlation of earthquake source parameters inferred from dynamic rupture simulations, *J. Geophys. Res.* **115,** no. 3, B03304, doi: 10.1029/2009JB006689.

Schmedes, J., R. J. Archuleta, and D. Lavallée (2012). A kinematic rupture model generator incorporating spatial interdependency of earthquake source parameters, *Geophys. J. Int.* **192,** no. 3, 1116–1131, doi: 10.1093/gji/ggs021.

Shi, Z., and S. M. Day (2013). Rupture dynamics and ground motion from 3-D rough-fault simulations, *J. Geophys. Res.* **118,** no. 3, 1122–1141, doi: 10.1002/jgrb.50094.

Somerville, P. (1999). Characterizing crustal earthquake slip models for the prediction of strong ground motion, *Seismol. Res. Lett.* **70,** no. 1, 59–80, doi: 10.1785/gssrl.70.1.59.

Song, S. G., and L. A. Dalguer (2013). Importance of 1-point statistics in earthquake source modelling for ground motion simulation, *Geophys. J. Int.* **192,** no. 3, 1255–1270, doi: 10.1093/gji/ggs089.

Song, S. G., and P. Somerville (2010). Physics-based earthquake source characterization and modeling with geostatistics, *Bull. Seismol. Soc. Am.* **100,** no. 2, 482–496, doi: 10.1785/0120090134.

Song, S. G., A. Pitarka, and P. Somerville (2009). Exploring spatial coherence between earthquake source parameters, *Bull. Seismol. Soc. Am.* **99,** no. 4, 2564–2571, doi: 10.1785/0120080197.

Stein, S., and M. Wysession (2002). *An Introduction to Seismology, Earthquakes, and Earth Structure*, Blackwell Science, Malden, Massachusetts.

Tinti, E., E. Fukuyama, A. Piatanesi, and M. Cocco (2005). A kinematic source-time function compatible with earthquake dynamics, *Bull. Seismol. Soc. Am.* **95,** no. 4, 1211–1223, doi: 10.1785/0120040177.

Townend, J., and M. D. Zoback (2000). How faulting keeps the crust strong, *Geology* **28,** no. 5, 399–402, doi: 10.1130/0091-7613(2000)28<399:HFKTCS>2.0.CO;2.

Tsutsumi, A., and T. Shimamoto (1997). High-velocity frictional properties of gabbro, *Geophys. Res. Lett.* **24,** no. 6, 699–702, doi: 10.1029/97GL00503.

Uchide, T., and S. Ide (2007). Development of multiscale slip inversion method and its application to the 2004 mid-Niigata Prefecture earthquake, *J. Geophys. Res.* **112,** no. B6, B06313, doi: 10.1029/2006JB004528.

Wang, J. (2008). One-dimensional dynamical modeling of earthquakes: A review, *Terr. Atmos. Ocean. Sci.* **19,** no. 3, 183–203, doi: 10.3319/TAO.2008.19.3.183(T).

Wesnousky, S. G. (2008). Displacement and geometrical characteristics of earthquake surface ruptures: Issues and implications for seismic-hazard analysis and the process of earthquake rupture, *Bull. Seismol. Soc. Am.* **98,** no. 4, 1609–1632, doi: 10.1785/0120070111.

Yoffe, E. H. (1951). LXXV. The moving griffith crack, *Phil. Mag. Series 7* **42,** no. 330, 739–750.

Zhao, L., P. Chen, and T. H. Jordan (2006). Strain Green's tensors, reciprocity, and their applications to seismic source and structure studies, *Bull. Seismol. Soc. Am.* **96,** no. 5, 1753–1763, doi: 10.1785/0120050253.

Zheng, G., and J. R. Rice (1998). Conditions under which velocity-weakening friction allows a self-healing versus a cracklike mode of rupture, *Bull. Seismol. Soc. Am.* **88,** no. 6, 1466–1483.

Department of Geophysics
Stanford University
397 Panama Mall
Stanford, California, 94305
dtrugman@lanl.gov